THE JOURNAL OF PHYSICAL CHEMISTRY C

Article

Interface Chemistry of Contact Metals and Ferromagnets on the Topological Insulator BiSe

Lee Adam Walsh, Christopher M. Smyth, Adam T. Barton, Qingxiao Wang, Zifan Che, Ruoyu Yue, Jiyoung Kim, Moon J. Kim, Robert M. Wallace, and Christopher L Hinkle

J. Phys. Chem. C, **Just Accepted Manuscript** • DOI: 10.1021/acs.jpcc.7b08480 • Publication Date (Web): 02 Oct 2017

ACS Publications

The Journal of Physical Chemistry C is published by the American Chemical Society. 1155 Sixteenth Street N.W., Washington, DC 20036

Interface Chemistry of Contact Metals and Ferromagnets on the Topological Insulator Bi_2Se_3

Lee A. Walsh,[1] Christopher M. Smyth, Adam T. Barton, Qingxiao Wang, Zifan Che, Ruoyu Yue, Jiyoung Kim, Moon J. Kim, Robert M. Wallace, and Christopher L. Hinkle*

Department of Materials Science and Engineering, University of Texas at Dallas, Richardson, TX 75080, United States

** Corresponding author email: chris.hinkle@utdallas.edu; Phone: +1 (972) 883-5711*

[1] Current address: Tyndall National Institute, University College Cork, Lee Maltings, Prospect Row, Cork, Ireland

Abstract

The interface between the topological insulator Bi_2Se_3 and deposited metal films is investigated using x-ray photoelectron spectroscopy including conventional contact metals (Au, Pd, Cr, and Ir) and magnetic materials (Co, Fe, Ni, $Co_{0.8}Fe_{0.2}$, and $Ni_{0.8}Fe_{0.2}$). Au is the only metal to show little or no interaction with the Bi_2Se_3, with no interfacial layer between the metal and the surface of the TI. The other metals show a range of reaction behaviors with the relative strength of reaction (obtained from the amount of Bi_2Se_3 consumed during reaction) ordered as: Au < Pd < Ir < Co ≤ CoFe < Ni < Cr < NiFe < Fe, in approximate agreement with the behavior expected from the Gibbs free energies of formation for the alloys formed. Post metallization anneals at 300°C in vacuum were also performed for each interface. Several of the metal films were not stable upon anneal and desorbed from the surface (Au, Pd, Ni, and $Ni_{0.8}Fe_{0.2}$), while Cr, Fe, Co, and $Co_{0.8}Fe_{0.2}$ showed accelerated reactions with the underlying Bi_2Se_3, including inter-diffusion between the metal and Se. Ir was the only metal to remain stable following anneal, showing no significant increase in reaction with the Bi_2Se_3. This study reveals the nature of the metal-Bi_2Se_3 interface for a range of metals. The reactions observed must be considered when designing Bi_2Se_3 based devices.

Introduction

Topological Insulators (TIs) are a class of material with topologically protected surface (or edge) states.[1] These surface states have properties such as spin-momentum locking[2] that may enable spin-polarized and defect-tolerant transport, making TIs attractive for a variety of applications, including spin-transfer torque non-volatile memory[3] and low-power FETs.[4-5] The most widely studied topological insulators are the three-dimensional TIs including Bi_2Se_3, with a range of reports on its behavior and epitaxial growth.[6-10] These materials have a layered structure with each unit cell (known as a quintuple layer) composed of five alternating layers of X-M-X-M-X (M is the metal and X is the chalcogen). The implementation of TI-based devices of course requires the deposition of metal contacts. Recent theoretical work by *Spataru et al.* has predicted that certain metals hybridize with the surface states, interrupting their topologically protected nature.[11] Additionally, due to the opposite surface state wavefunction overlap between the top and bottom surfaces, Bi_2Se_3 films below six quintuple layers (QLs) have the bulk electronic structure (and surface states) perturbed.[6] As a result, any device designs utilizing thin TI layers (<10 QLs) must consider chemical reactions between the contact metal and the TI which may consume some of the topmost QLs, underscoring the importance of the choice of contact metal.

Bi_2Se_3 based devices in the literature have employed a range of contact metals including Ti,[12] Cr,[13] Pd,[14] and Au.[15] Additionally, coupling TIs with ferromagnets have applications for memory and logic and, for these devices a ferromagnetic material is deposited on the TI, usually permalloy ($Ni_{0.8}Fe_{0.2}$) or CoFeB.[3, 16] Recent work by *de Jong et al.* utilized ARPES measurements to study the impact of Fe, Nb, and Ag on the band structure of $Bi_{1.5}Sb_{0.5}Te_{1.7}Se_{1.3}$,[17] which showed a downward band bending following the deposition of each

metal. Core level spectra also showed the interaction between the metal and the TI, with Ag found to even intercalate into the van der Waals gap and react by substitution of Se and/or Te. A similar study by *Ye et al.* studied the band bending in Bi_2Se_3 following the deposition of transition metals including Cr, Fe, Ni, and Co, using ultraviolet photoelectron spectroscopy and x-ray photoelectron spectroscopy (XPS).[18] While evidence of interfacial reaction and the formation of metallic Bi was observed in the cases of Cr and Ni there was no peak deconvolution performed to fully understand the chemistry of the interface.

In this study, we investigate the interface chemistry for a range of conventional contact metals (Ni, Pd, Au, Cr, and Ir) and some ferromagnetic materials (Ni, Fe, Co, $Ni_{0.8}Fe_{0.2}$, and $Co_{0.8}Fe_{0.2}$) all deposited by electron beam evaporation on Bi_2Se_3. Firstly, we will present characterization of the molecular beam epitaxy (MBE) grown Bi_2Se_3, and the effectiveness of the protective Se cap used to maintain a pristine surface during *ex-situ* transfer. Next, we will present the XPS spectra of the films after the deposition of each metal with a description of the behavior observed in each. A discussion section follows in which we discuss the trends observed for the metal-Bi_2Se_3 interaction and we group the metals by those which show similar behavior. We will conclude by discussing which metals seem most suitable for use as contacts based on the degree of interfacial reactions observed.

Methods

Molecular beam epitaxy growth of Bi_2Se_3. C-plane sapphire substrates were purchased from University Wafer.[19] Bi_2Se_3 growth was performed in a VG-Semicon V80H MBE system that is part of a three-chamber MBE cluster system with each of the growth chambers interconnected with ultra-high vacuum (UHV) transfer tubes (base pressure = 10^{-11} mbar).[20] The TI growth

chamber is equipped with Knudsen effusion cells for the evaporation of Se and Bi, and *in-situ* reflection high energy electron diffraction (RHEED) for characterization of the grown films. Bi_2Se_3 was grown on 1 cm^2 c-axis oriented sapphire substrates which were sequentially cleaned in acetone, methanol, and isopropyl alcohol for 10 minutes each. The sapphire samples were then loaded into the system and annealed at 600°C for 90 mins, and 750°C for 10 mins to degas and clean the surface before being cooled to the growth temperature. Before each growth, the Bi and Se sources were outgassed for 2 h. The Bi_2Se_3 films were grown using a two-step process[9] (110°C as a nucleation step, and then 320°C for the remainder of the growth) with a Se:Bi flux of 20:1. The growth rate for Bi_2Se_3 on sapphire was determined to be ~0.5 QL/min from transmission electron microscopy (TEM). The quality of the MBE grown material is highly reproducible and, to minimize the variability in this study, the samples were grown and capped at the same time in only two growth runs (half of the total samples in each run) and stored in an inert environment until needed. Full characterization of the grown material using XPS, Raman, TEM, and STM has been repeated for several of the samples in both growth runs, and they all exhibit the same grain size, crystallinity, and chemical composition.

Samples for *ex-situ* XPS analysis were Se capped at room temperature for 1 hour *in-situ* after growth, to achieve a capping layer ~40 nm thick. This was used to prevent oxidation and the adsorption of environmental contaminants on the Bi_2Se_3 surface during transfer to the XPS instrument. For TEM analysis, a ~20 nm thick Bi film was deposited *in-situ* after growth as the capping layer. 20 nm of TiN was used as the capping layer for the permalloy on Bi_2Se_3 TEM sample.

Desorption of the Se cap and metal deposition. Samples were subsequently transferred into a UHV cluster tool for decapping, metal deposition, and XPS analysis. This tool is described in

detail elsewhere.[21] Decapping was performed by thermal anneal at 190°C for 60 minutes under a base pressure of 10^{-9} mbar. All metal depositions were performed by electron beam evaporation at a base pressure of 10^{-9} mbar after significant outgassing of the metal sources. The targeted thickness for the metal films on Bi_2Se_3 was 1.5 nm, and 20 nm for the metal reference films deposited on Si. The specific procedures employed for metal deposition are described elsewhere.[22]

XPS characterization and peak fitting. XPS for all samples was carried out using a monochromated Al Kα source and an Omicron EA125 hemispherical analyzer with resolution of ±0.05 eV. The analyzer acceptance angle of 8°, takeoff angles of 45° and 75° (angle-resolved (AR) XPS), and pass energy of 15 eV were utilized in this study. In the AR XPS spectra by increasing the electron takeoff angle the effective sampling depth into the material is also increased providing a more bulk sensitive measurement. The AR spectra were acquired to understand the relative position of any new chemical state relative to the Bi_2Se_3 film. The analyzer was calibrated using sputter cleaned Au, Cu, and Ag foils, as is outlined in ASTM E2108.[23] The stoichiometries extracted from XPS are calculated using the appropriate relative sensitivity factors for the Bi 5*d*, Se 3*d*, Fe 3*p*, Co 2*p*, and Ni 2*p* core levels (1.259, 0.722, 0.301, 2.142, and 2.435, respectively).[24] The stoichiometry ratios calculated are accompanied by a ±0.2 error.

The core level spectra were deconvoluted using the curve-fitting software AAnalyzer.[25] Metallic chemical states were fit with the asymmetric double Lorentzian line shape, while non-metallic chemical states were fit with Voigt line shapes. An active Shirley background subtraction was employed in fitting all spectra.[25] In order to accurately detect the presence of

additional features in any of the core levels, all fits were performed with comparison to reference samples, i.e. using the bare Bi_2Se_3 after removal of the Se cap as a reference for the Bi 5*d* and Se 3*d*, and using thick metal references for the metallic chemical states. The peak separations and full-width half-maxima (FWHM) of the reference peaks are kept constant to maintain consistency. Additionally, for the metallic peaks the asymmetry factors are kept constant. Small deviations (<0.1 eV) in the absolute binding energy (BE) of the chemical states are allowed to account for small E_F shifts after metal deposition. The XPS studies were repeated at least twice for Au, Cr, and Ir as spot checks to ensure that the observed reactions were reproducible.

Other characterization. Raman spectra acquisition was performed with a Renishaw confocal Raman system employing a laser wavelength of 532 nm, laser power of 0.22 mW and spot size of 500 nm. TEM cross-sectional samples were made by FIB-SEM Nova 200 with a lift-out method. A JEM-ARM200F transmission electron microscope operated at 200 kV with probe aberration corrector was used for Bi_2Se_3 cross-section imaging. X-ray diffraction (XRD) characterization employed a Rigaku Ultima III X-ray diffractometer system. Data were acquired in a symmetric geometry (2θ-θ scan) using parallel beam optics.

Results and Discussion

In-situ RHEED of the as-grown Bi_2Se_3 on sapphire taken along the [10-10] direction is shown in Figure 1a. The observation of sharp streaks indicates the smoothness and crystallinity of the film and the lattice spacing extracted matches that expected for bulk Bi_2Se_3 (4.11±0.12 Å). Raman measurements in Figure 1b from a thick (40 QL) MBE-grown sample show the characteristic Raman modes at 131 cm^{-1} (E^2_{1g}) and 173 cm^{-1} (A^2_{1g}).[26] Cross-sectional TEM

images of Bi_2Se_3 grown on sapphire are shown in Figure 1c. The layered structure is clearly observed with a van der Waals gap between each QL. XRD spectra in Figure 1d show the (006) peak for the Bi_2Se_3, confirming that the film aligns to the (001) sapphire along the (00l) direction.

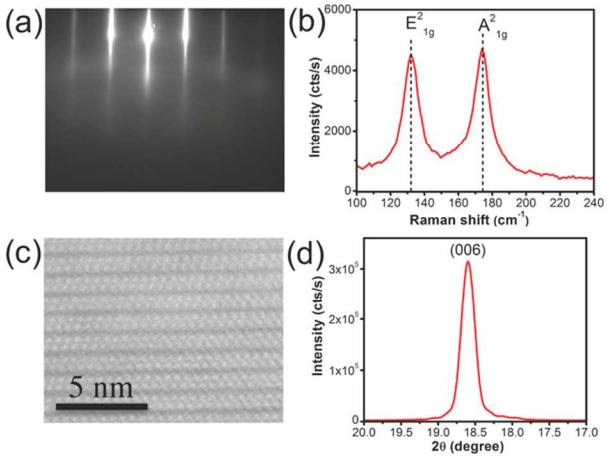

Figure 1: (a) RHEED pattern of Bi_2Se_3 along the [10-10] direction showing a streaky pattern indicating a flat, crystalline film. (b) Raman showing the expected Bi_2Se_3 modes. (c) TEM image of Bi_2Se_3 grown on sapphire. (d) XRD spectra of the film showing the (006) diffraction peak.

Bi_2Se_3 films oxidize readily upon air exposure.[27] This oxidation results in electron doping of the TI surface, although it does not impact the topology of the surface states.[28] In order to prevent oxidation and the adsorption of other atmospheric contaminants, the *in-situ* deposition of an amorphous Se cap immediately after Bi_2Se_3 growth has been used to protect the surface and enable *ex-situ* transfer between the growth chamber and the XPS instrument.[29] The removal of this Se cap is then performed through low-temperature (190°C) thermal annealing to recover an oxygen and carbon-free Bi_2Se_3 surface. XPS spectra of the Bi 5*d* core level (Figure 2a) with the Se cap shows the absence of any Bi related features, while removing the Se cap reveals a sharp

Bi doublet. The Se 3*d* shows a shift after decap consistent with the binding energy (BE) difference between Se-Se bonding and Bi_2Se_3. No oxide is detected in either spectra. The O 1*s* spectra in Figure 2b show no detectable signal in the Se-capped or bare Bi_2Se_3 sample, while the C 1*s* spectra shows a small adventitious carbon peak in the capped sample and the absence of any detectable C for the decapped surface. The broad peak centered at 282.8 eV is related to a Se Auger feature.[30] The cleanliness of the Bi_2Se_3 surface after decap confirms the effectiveness of the Se cap.

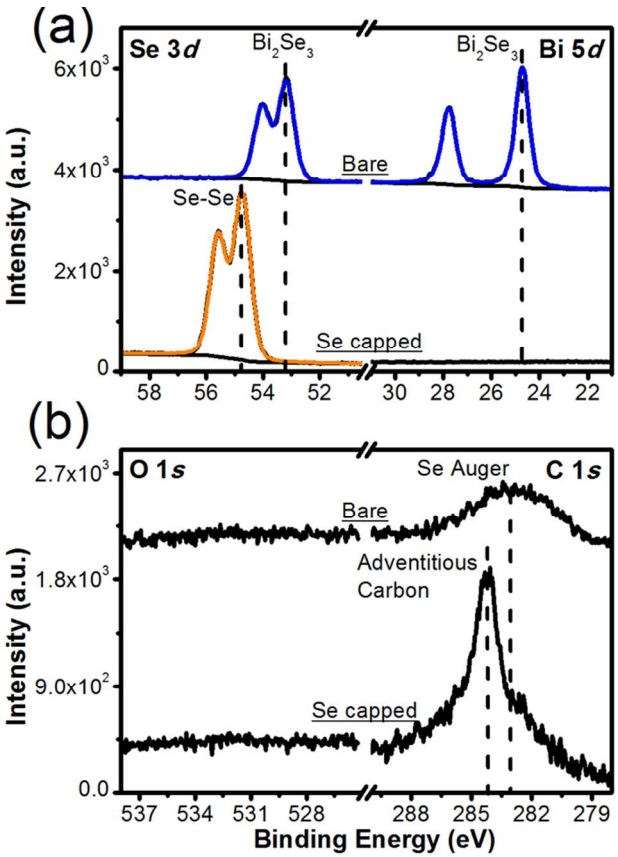

Figure 2: XPS spectra of (a) the Se 3*d* and Bi 5*d* core levels of a sample before and after the removal of the Se protective cap. (b) O 1*s* and C 1*s* core levels showing the effectiveness of the Se cap in protecting the Bi_2Se_3 surface from atmospheric oxidation and carbon adsorption.

Au – Bi_2Se_3

We begin with Au which, as previously mentioned, *Spataru et al.* predicted (as well as graphene) would not hybridize with the TI surface states to disrupt the spin-momentum locking.[11] Upon deposition of 1.5 nm of Au, we observe the appearance of an additional feature at higher BE, ~58 eV in the Se 3*d* spectra shown in Figure 3a which is the Au 5*p* core level (not an additional Se state).[31] No other change in the Se 3*d* is observed following Au deposition, or in the more bulk-sensitive AR spectra, indicating no detectable Au-Se bond formation. In the Bi 5*d* spectra a small feature is observed at lower BE with a peak position (23.8 eV) consistent with a metallic Bi (Bi^0) state. In the AR spectra, this feature decreases relative to the Bi_2Se_3 peak as a function of increasing take-off angle, indicating it is surface localized with respect to the Bi_2Se_3 film. Bi out-diffusion has been previously observed for In_2Se_3 grown on Bi_2Se_3.[32] Upon Au deposition, some of the Bi diffuses to the surface forming a Bi-rich state. The Au 4*f* peak is shifted ~0.1 eV to higher BE (relative to a Au reference) as shown in Figure 3b. There is no substantial change in lineshape between the two spectra as confirmed in the supplemental information Figure S1a. This, along with the lack of any Au-Se interaction in the Se 3*d* indicates no chemical interaction is detected between Au and Bi_2Se_3. This is further confirmed in the TEM image shown in Figure 4, where no interfacial layer is observed between the deposited Au layer and the Bi_2Se_3 surface. This agrees with thermodynamic data which indicates a reaction between Bi_2Se_3 and Au is not favorable, as $\Delta G^\circ_{f,Bi2Se3}$ = -146.6 kJ.mol^{-1} and $\Delta G^\circ_{f,AuSe}$ = -32.0 kJ.mol^{-1}.[33] All standard Gibbs free energies are reported per selenium atom. The Au-Bi_2Se_3 behavior is consistent with the lack of chemical interaction previously observed between Au and other layered materials.[22, 31] Combined with theoretical simulations which predict no Schottky barrier

between Au and Bi_2Se_3,[11] this identifies Au to be an excellent choice for contacts based on the conservation of the inert nature and topological properties of the Bi_2Se_3 surface.

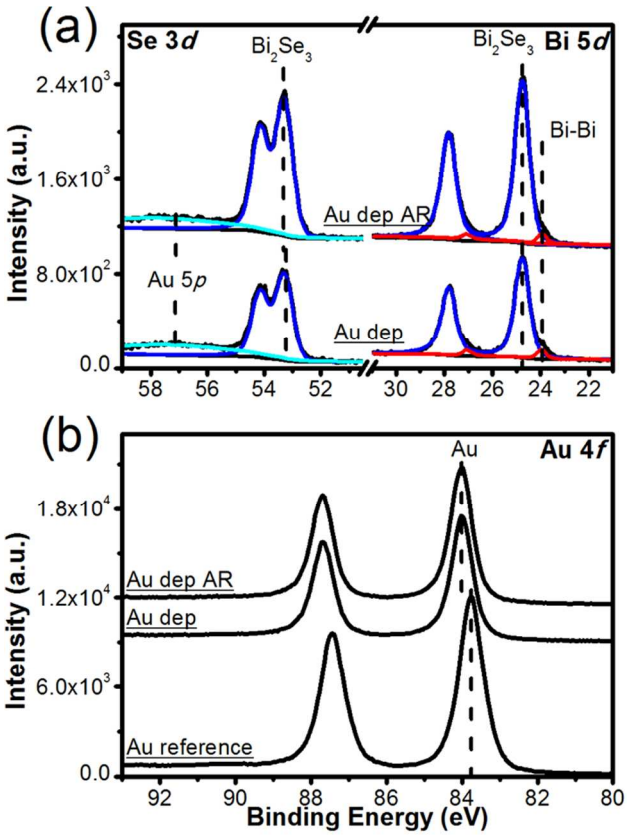

Figure 3: XPS spectra of (a) the Se 3*d* and Bi 5*d* core levels of Bi_2Se_3 after Au deposition. Note the peak at ~57 eV is an Au auger feature. (b) Au 4*f* core level showing no change in lineshape and a small shift to higher BE when compared to a thick Au reference film.

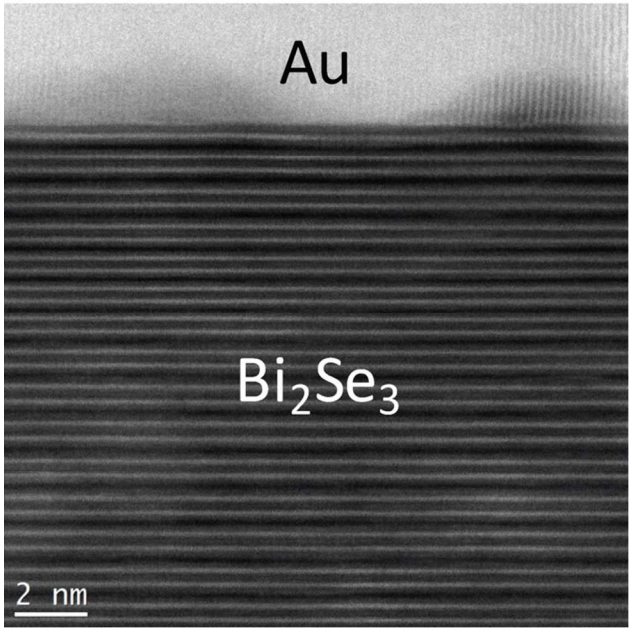

Figure 4: Cross-sectional TEM image of Au on Bi_2Se_3 showing no evidence of an interfacial layer, in agreement with the XPS spectra.

Pd – Bi_2Se_3

Pd contacts have been used in several previous studies of Bi_2Se_3 based devices.[34-35] Simulations have predicted that unlike Au, Pd hybridizes with the Bi_2Se_3 surface states resulting in the disruption of the surface Dirac cone.[11] The core level spectra in Figure 5a show significant interaction between Pd and Bi_2Se_3 following deposition. A peak is observed at lower BE in the Bi 5*d* spectra, at a position 0.1 eV higher in BE than the peak observed for Au on Bi_2Se_3. However, as shown in Figure S2a, the peak is not at the same BE as would be expected for metallic Bi, indicating it is likely due to a reduced (i.e. lower oxidation state) Bi_2Se_x. There is also the possibility that it is related to a $Pd_xBi_ySe_z$ phase which has been previously explored as a superconducting material.[36] In the Se 3*d* spectra, an additional feature appears at higher BE attributable to either $PdSe_x$ or $Pd_xBi_ySe_z$, both of which are consistent with the respective

electronegativites of Bi (2.02), Se (2.55), and Pd (2.20).[37] There is a subtle change in the Pd 3*d* lineshape (Figure 5b) when a thick (~20 nm) Pd reference and Pd on Bi_2Se_3 are compared, along with a shift of ~0.65 eV to higher BE. The change in lineshape can be clearly observed when the spectra are normalized and aligned, as shown in Figure S3a. The as-deposited Pd on Bi_2Se_3 has a more symmetric lineshape suggesting the Pd is not present as a pure metal (metals typically have asymmetric line shapes commonly attributed to core-hole screening effects),[38] but rather has reacted with the Bi_2Se_3 to possibly form the aforementioned $PdSe_x$ or $Pd_xBi_ySe_z$. A previous study investigated the ability to alloy Pd into Bi_2Se_3 layers using post metallization anneals between 200°C and 300°C to produce a superconducting phase.[34] No significant chemical analysis was reported in that work and therefore limited comparisons can be drawn from the literature, apart from showing that Pd does interdiffuse and react significantly with Bi_2Se_3. In our study, a nearly complete desorption of the Pd or $Pd_xBi_ySe_z$ was observed following a 300°C post-deposition anneal, as shown in Figure S3b. It does not appear that the Pd diffused into or alloyed with the Bi_2Se_3, as a detectable Pd signal would still be expected if this were the case.

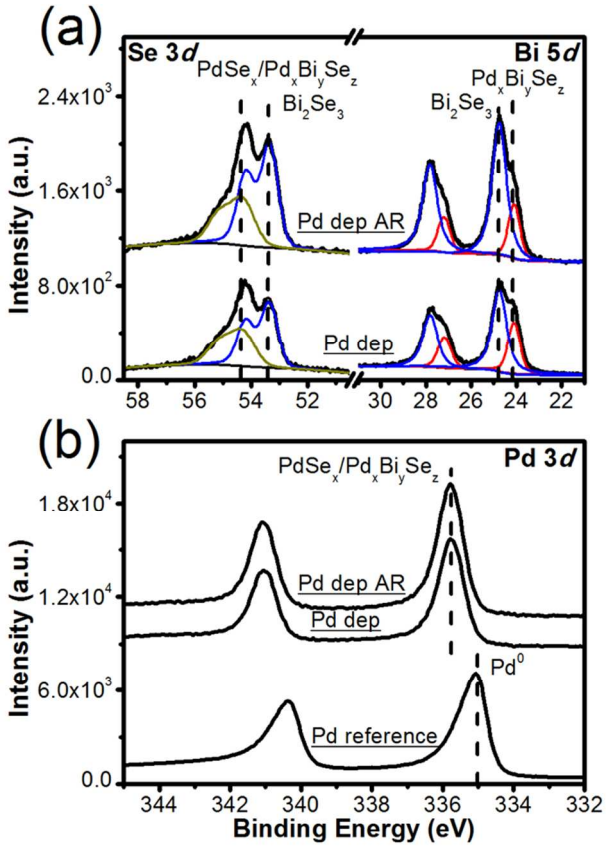

Figure 5: XPS spectra of (a) the Se 3*d* and Bi 5*d* core levels of Bi_2Se_3 after Pd deposition. (b) Pd 3*d* core level of a thick Pd reference and Pd as-deposited on Bi_2Se_3.

Ir – Bi_2Se_3

Iridium has been previously studied as a transition metal dopant in Bi_2Se_3.[39] IrBiSe crystals have been grown using the self-flux method and tested as a non-magnetic half-metal with applications in spintronic devices.[40] Upon deposition of Ir on the Bi_2Se_3 surface, a peak is observed at lower BE in the Bi 5*d* spectra (Figure 6a), at a similar energy to the peak observed after Pd deposition. This peak is likely due to the formation of $Ir_xBi_ySe_z$, consistent with the similar electronegativites of Ir (2.20) and Pd (2.20).[37] The larger peak intensity compared to Pd indicates a stronger interaction. The decrease in the $Ir_xBi_ySe_z$ relative to the Bi_2Se_3 feature in the bulk-sensitive AR spectra indicates that it is located at the Ir/Bi_2Se_3 interface. The Se 3*d* core

level of the same samples show the appearance of a broad feature at ~54.5 eV which can be attributed to the $Ir_xBi_ySe_z$. An alternative explanation could be behavior similar to that observed for Ir deposited on transition metal dichalcogenide films, where a substantial interaction peak (identified as IrS_x or $IrSe_x$) is observed via the reduction of MoS_2 or WSe_2.[22, 31] In the Bi_2Se_3 system, this would result in Ir and Se reacting to form an $IrSe_x$ species with the reduction of Bi_2Se_3 to form Bi_2Se_x or Bi^0. However, in a study of Ir metal deposition on WSe_2, the $IrSe_x$ feature was reported at a higher BE (55.43 eV as compared to 54.41 eV in our work) indicating that the reaction observed in our XPS spectra is more likely attributed to the aforementioned $Ir_xBi_ySe_z$ formation. This $Ir_xBi_ySe_z$ peak decreases slightly in the AR spectra suggesting that it may be slightly more surface sensitive than the Bi_2Se_3, and thus located at the Ir/Bi_2Se_3 interface. After a 300°C anneal for 1 hour the $Ir_xBi_ySe_z$ peak area in the Bi *5d* core level spectrum increases slightly. At the same time, the total area of the Se 3*d* peak and the ratio of the $Ir_xBi_ySe_z$ peak to the Bi_2Se_3 peak stay roughly constant, suggesting no substantial increase in reaction between Ir and Bi_2Se_3.

Figure 6b shows the Ir 4*f* spectra for a thick (~20 nm) Ir reference film and the Ir thin films on Bi_2Se_3. A small shift of ~0.1 eV to lower BE is observed between the Ir reference and the Ir film as-deposited on Bi_2Se_3. The peak lineshape is also subtly different as shown in the normalized spectra in Figure S2a, with a slight broadening to higher BE, consistent with an $Ir_xBi_ySe_z$ feature. This again indicates that the deposited Ir is not a completely metallic film, but rather that it has interacted with the underlying Bi_2Se_3 to form $Ir_xBi_ySe_z$.[39-40] No further BE shift or change in lineshape is observed after anneal. The diffusion of each element is also observed in Figure S4d where the peak area of each feature is shown as a function of the experimental step. The Bi 5*d* and Se 3*d* peaks are shown to decrease in area due to the attenuation of the deposited Ir, although

the Bi is attenuated less due to the formation of the $Ir_xBi_ySe_z$ layer. The changes in the area of the Bi, Se, or Ir peaks after anneal are small, suggesting minimal interdiffusion as a function of anneal. The chemical states of the compounds formed are stable up to 300°C.

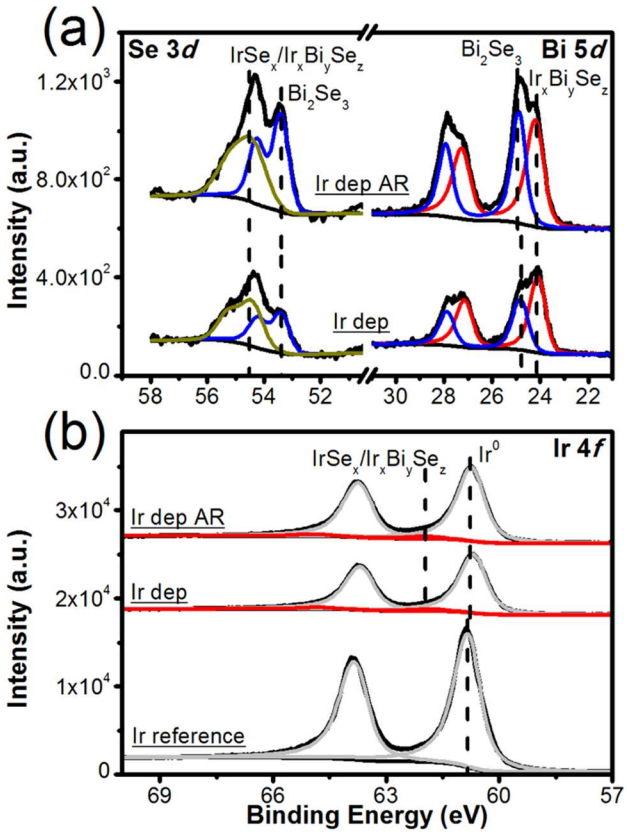

Figure 6: XPS spectra of (a) the Se 3*d* and Bi 5*d* core levels of Bi_2Se_3 after Ir deposition. (b) Ir 4*f* core level of a thick Ir reference, Ir as-deposited on Bi_2Se_3 and following 300°C anneal.

Cr – Bi_2Se_3

Cr is typically used as a so-called adhesion or wetting layer for depositing contacts on topological insulators and other inert materials such as transition metal dichalcogenides.[41-42] This aids in the adhesion of other metals such as Au to the TI surface. Cr has also been investigated as a possible magnetic dopant in Bi_2Se_3 which can perturb the surface states to open up an energy gap.[43] Upon Cr deposition, we observe a peak at lower BE in the Bi 5*d* spectra

(Figure 7a) at a BE position (23.7 eV) consistent with Bi^0, as confirmed in Figure S2b. The bulk-sensitive AR spectra confirm this to be surface localized, suggesting the out-diffusion of Bi, possibly due to its surfactant properties.[44] The Bi 5*d* peak area decreases significantly upon anneal, though no significant change in chemical state is observed. A previous study investigated the deposition of Cr on Bi_2Se_3 and a similar metallic Bi feature was reported although no Se spectra were shown.[18] After Cr deposition, a peak appears in the Se 3*d* spectrum at slightly higher BE than the bulk Bi_2Se_3 due to a Cr-Se interaction ($CrSe_x$). Thermodynamic data suggests that reaction between Bi_2Se_3 and Cr is favorable, as $\Delta G^{\circ}_{f,Cr2Se3}$ = -175.1 $kJ.mol^{-1}$.[45] This behavior is similar to that observed in the Cr-MoS_2 and Cr-Wse_2 systems where Cr reacts to form a Cr_xSe_y or CrS_x and W or Mo metal.[22, 31] After annealing at 300°C under UHV, the intensity of both the total Se 3*d* core level and Cr-Se state increases dramatically relative to the Bi 5*d*, indicating significant Se out-diffusion. The Cr $2p_{3/2}$ spectra are shown in Figure 7b. The lineshape of the as-deposited Cr is similar to a thick Cr reference film, with the addition of a slight broadening at higher BE, caused by the presence of an additional feature related to $CrSe_x$ (see Figure S5a). After a 300°C anneal, the $CrSe_x$ peak intensity increases significantly, consistent with the associated chemical state in the Se 3*d* spectrum and the increased interaction between Cr and Bi_2Se_3. This can also be observed in Figure S5b where the peak area of each feature is shown as a function of the experimental step. The Bi 5*d* and Se 3*d* peaks are shown to decrease in area due to the attenuation of the deposited Cr, although the Bi is attenuated less due to the formation of the Bi^0 layer at the interface.

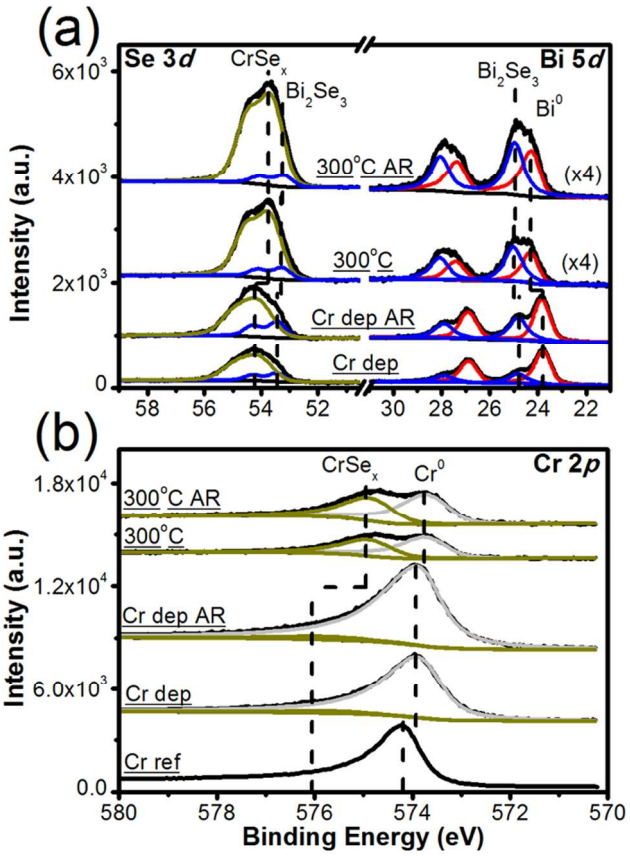

Figure 7: XPS spectra of (a) the Se 3*d* and Bi 5*d* core levels of Bi_2Se_3 after Cr deposition and following a 300°C anneal. Note the Bi 5*d* core levels for the sample following a 300°C anneal have been multiplied by a factor of 4 for easier comparison. (b) Cr $2p_{3/2}$ spectra of a Cr reference film, Cr deposited on Bi_2Se_3 and the same sample following a 300°C anneal.

Fe – Bi_2Se_3

One of the main proposed applications of topological insulators is in non-volatile memory where the spin-transfer torque generated by current flowing through the TI surface states is used to switch the magnetization of a ferromagnet. Of course Fe is a typical component in the ferromagnetic layers ($Ni_{0.8}Fe_{0.2}$, $Co_{0.8}Fe_{0.2}$) used in such TI/ferromagnet structures.[3] It is also of interest as a magnetic interstitial or surface dopant enabling the opening of a gap in the surface

states (observed for Fe concentrations in excess of 5%), and the subsequent observation of a massive Dirac Fermion.[46]

Upon Fe deposition, the Bi 5*d* spectrum in Figure 8a is dominated by a lower BE feature with a peak position consistent with metallic Bi as confirmed in Figure S2b. The Bi_2Se_3 feature is barely detectable, but becomes more pronounced in the bulk-sensitive AR spectra, confirming the metallic Bi layer is surface localized. After the 300°C anneal, there is no further change in this feature. The corresponding Se 3*d* spectrum is dominated by the nearby Fe 3*p* core level following deposition, although there is a low intensity feature present at higher BE with a peak position suggesting $FeSe_x$. The narrow FWHM of this peak indicates the formation of a crystalline layer, which has been previously observed with TEM as the formation of a layered, crystalline $FeSe_{0.92}$ film at the interface of Fe and Bi_2Se_3.[47] After the 300°C anneal, a substantial change is observed with the spectra now dominated by the $FeSe_x$ peak and a substantial decrease in the Fe 3*p*. Additionally, a chemical state which suggests Se-Se bonding appears at ~55.0 eV. The suppression of the Bi_2Se_3 feature in the Bi 5*d* indicates that the top 2-3 QL of Bi_2Se_3 are fully consumed to form $FeSe_x$ after anneal. This Fe-Se reaction is thermodynamically favorable as $\Delta G^{\circ}_{f,\,Fe3Se4} = -244.0\ kJ.mol^{-1}$.[33]

ARXPS shows that the Fe-Se is more surface localized indicating interdiffusion between Fe and Se to form $FeSe_x$ at the Bi_2Se_3 surface. The as-deposited Fe $2p_{3/2}$ spectra (Figure 8b) is similar to that observed for a thick Fe reference film, confirmed by normalized spectra in Figure S6a. Upon anneal the peak broadens to higher BE, due to the presence of an Fe-Se feature like that observed for Cr on Bi_2Se_3. The diffusion behavior of each element can be observed in Figure S6b where the area of each core level is shown as a function of the experimental step. The Bi 5*d* and Se 3*d* peaks are shown to decrease in area due to the attenuation of the deposited

Fe. A dramatic increase in the Se 3*d* area is observed following the anneal indicating preferential out-diffusion of Se and its conversion of the metallic Fe film to a mix of metallic Fe and $FeSe_x$, while the Bi peak area remains unchanged. If Se out-diffusion is occurring it would lead to an increase in thickness of the overlayer, but there is no simultaneous attenuation of the Bi 5*d*. This indicates significant intermixing between the metallic Bi and $FeSe_x$ or possible clustering of the Fe/$FeSe_x$ overlayer. The Fe $2p_{3/2}$ area decreases slightly after annealing, likely due to the increased interdiffusion of Fe and Se. A previous study also observed the formation of metallic Bi upon Fe deposition.[48] Their interpretation of the Se 3*d* spectra suggested no Fe-Se interaction, however, and may be attributed to interpreting the $FeSe_x$ feature as the metallic Fe 3*p* feature despite a significant BE shift from their own Fe 3*p* reference.

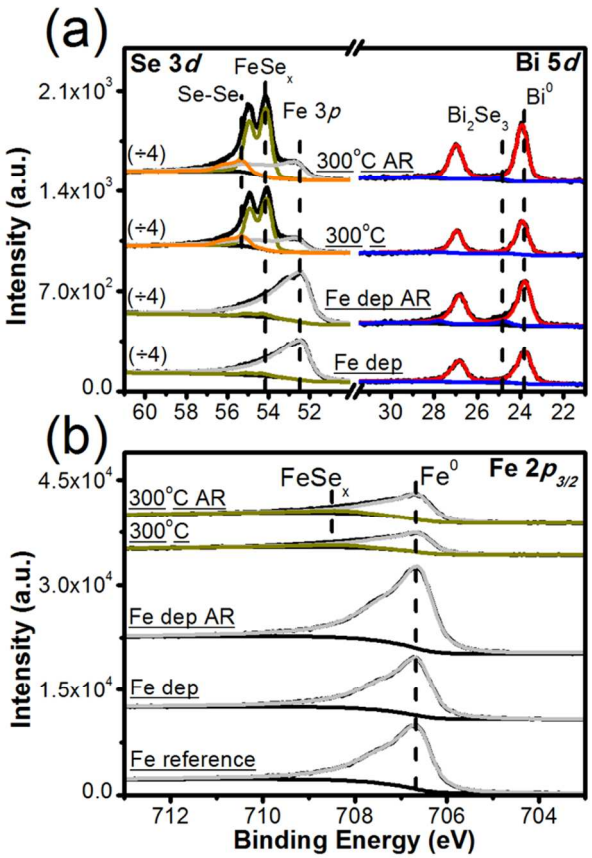

Figure 8: XPS spectra of (a) the Se 3*d* and Bi 5*d* core levels of Bi_2Se_3 after Fe deposition, and following a 300°C anneal. Note all the Se 3*d* spectra have been divided by a factor of 4 for easier comparison. (b) Fe $2p_{3/2}$ spectra of a Fe reference film, Fe deposited on Bi_2Se_3 and the same sample following a 300°C anneal.

Co – Bi_2Se_3

Co has applications as both a magnetic dopant[49] and as a component in CoFeB,[50] which is widely used as a magnetic layer in TI/ferromagnet structures. The Bi 5*d* spectra for Co deposited on Bi_2Se_3 are shown in Figure 9a. A peak is observed at lower BE in addition to the Bi_2Se_3 feature. When compared to a reference metallic Bi film we see that the peak is at 0.1 eV higher BE, whereas the Bi_2Se_3 peak position is consistent with that observed for other materials. This may indicate the formation of $Co_xBi_ySe_z$ as opposed to metallic Bi, a material which has

been grown previously with up to 10% Co incorporation.[49] Bulk-sensitive AR spectra confirm that this material is located on the surface of the Bi_2Se_3 film. Upon annealing, the $Co_xBi_ySe_z$ feature decreases slightly. In the Se 3*d* spectrum obtained after Co deposition a broad feature at 0.8 eV higher BE appears consistent with a Co-Se interaction. Given the respective electronegativities of Co (1.88), Se (2.55), and Bi (2.02),[37] this suggests a Se rich $CoSe_x$ or $Co_xBi_ySe_z$.[51] AR spectra confirm it is located above the Bi_2Se_3 probably at the Co/Bi_2Se_3 interface. A similar interaction has previously been reported for Co on Bi_2Te_3, with $CoTe_2$ formed at the interface.[52]

After anneal the intensity of the Se 3*d* core level increases dramatically, indicating significant Se out diffusion. As the Bi 5*d* core level intensity increases by a much smaller degree following anneal it suggests that the large peak observed in the Se 3*d* spectra is more likely $CoSe_x$ rather than $Co_xBi_ySe_z$. A narrowing of the $CoSe_x$ peak FWHM is also observed suggesting possible crystallization of the film. The Se 3*d* broadens to higher BE, indicating the formation of Se-Se bonds, consistent with the continued out-diffusion of Se from the Bi_2Se_3.

The Co $2p_{3/2}$ spectra are shown in Figure 9b. The as-deposited Co shows a similar peak position and lineshape as for a thick Co reference film as shown in Figure S7a. After annealing, the peak narrows slightly but otherwise shows no discernible change. This would indicate that the film is still metallic Co although when interpreted in combination with the Bi 5*d* and Se 3*d* spectra it does appear that a significant amount of the Co has reacted to form $CoSe_x$ and $Co_xBi_ySe_z$. It is possible that the $CoSe_x$/$Co_xBi_ySe_z$ partially crystallizes during annealing as the FWHM of the chemical state in the Se 3*d* spectrum attributed to $CoSe_x$/$Co_xBi_ySe_z$ decreases by ~20% after annealing.

The diffusion behavior of each element can be observed in Figure S7b where the peak area is shown as a function of the experimental step. The Bi 5*d* and Se 3*d* peaks are shown to decrease in area due to the attenuation of the deposited Co. A dramatic increase in the Se 3*d* area is observed following the anneal indicating Se out-diffusion and continued reaction with the Co, while the Bi peak area also increases very slightly. The Co $2p_{3/2}$ area decreases slightly after anneal likely due to the increased interdiffusion and reaction of Co and Se. Intermixing between Co and Bi_2Se_3 was previously proposed based on x-ray absorption spectra and the measurement of a 1.2 nm thick magnetic dead layer of Co when deposited on Bi_2Se_3.[53] A similar interfacial layer is observed for permalloy, another magnetic material, as will be shown later in this article.

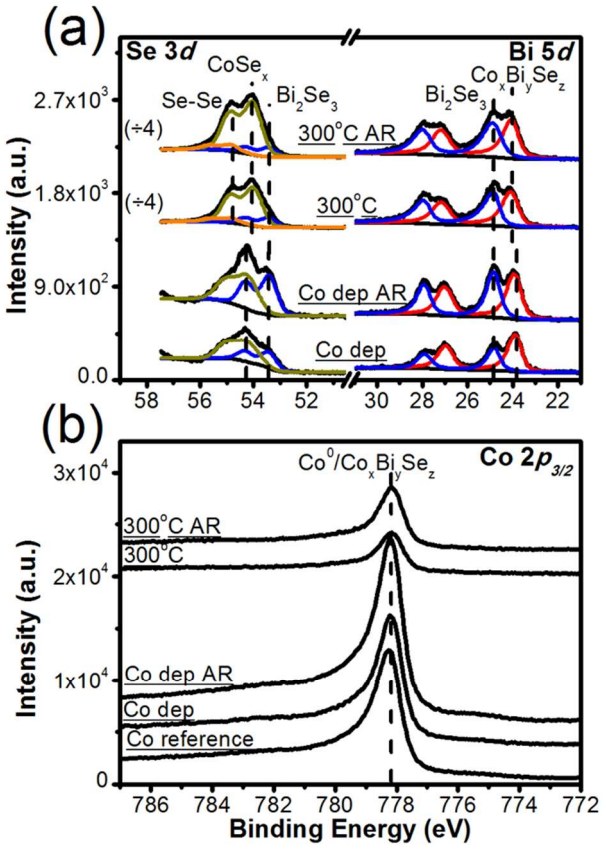

Figure 9: XPS spectra of (a) the Se 3*d* and Bi 5*d* core levels of Bi_2Se_3 after Co deposition and following a 300°C anneal. Note the Se 3*d* spectra after anneal have been divided by a factor of 4 for easier comparison. (b) The Co $2p_{3/2}$ for a Co reference film, Co as-deposited on Bi_2Se_3, and following a 300°C anneal.

$Co_{0.8}Fe_{0.2} – Bi_2Se_3$

As previously mentioned CoFeB is one of the most popular choices for ferromagnetic materials in ferromagnet/TI structures.[50] Boron was not available in our deposition system so we have here used $Co_{0.8}Fe_{0.2}$ (hereafter referred to simply as "CoFe") as an analog material to study the interface with Bi_2Se_3. The actual stoichiometry of the deposited film was determined from XPS fitting of the Co 2*p* and Fe 3*p* core levels as $Co_{0.76}Fe_{0.24}$. The XPS spectra of the Bi 5*d* and Se 3*d* core levels are shown in Figure 10a. The features observed in both core levels are almost

identical to those for Co on Bi_2Se_3, which is unsurprising given the material is 80% Co. While the Bi 5*d* behavior is identical to that when Co-only was deposited, there are a few differences in the Se 3*d*. An additional feature is observed at 52.5 eV, due to the Fe 3*p* core level which overlaps with the Se 3*d*. The same overlap was previously observed for Fe on Bi_2Se_3 in Figure 8a. The close overlap between $FeSe_x$ (54.1 eV) and $CoSe_x$ (54 eV) indicates that there is likely a mix of Co-Se and Fe-Se present in the Se 3*d* peak. If similar values of x for both $FeSe_x$ and $CoSe_x$ are assumed, it is reasonable to expect their associated chemical states in the Se 3*d* spectrum to exhibit nearly identical binding energies considering the similar electronegativities of Co and Fe (1.88 and 1.83, respectively).[37] The Co $2p_{3/2}$ shows a similar lineshape and peak position as for a Co reference film, as shown in Figure S8a. The Fe core levels are difficult to compare to Fe reference films due to the overlap between the Fe $2p_{3/2}$ and Co *LMM* Auger.[30] Similarly, the Fe 3*p* is overlapped with the Se 3*d*. The diffusion behavior of each element can be observed in Figure S8c where the peak area of each feature is shown as a function of the experimental step, with similar behavior to that of Co. In summary, the behavior observed for CoFe is very similar to that for Co on Bi_2Se_3, although there may be some additional $FeSe_x$ present which overlaps closely with the $CoSe_x$ so as to be indistinguishable.

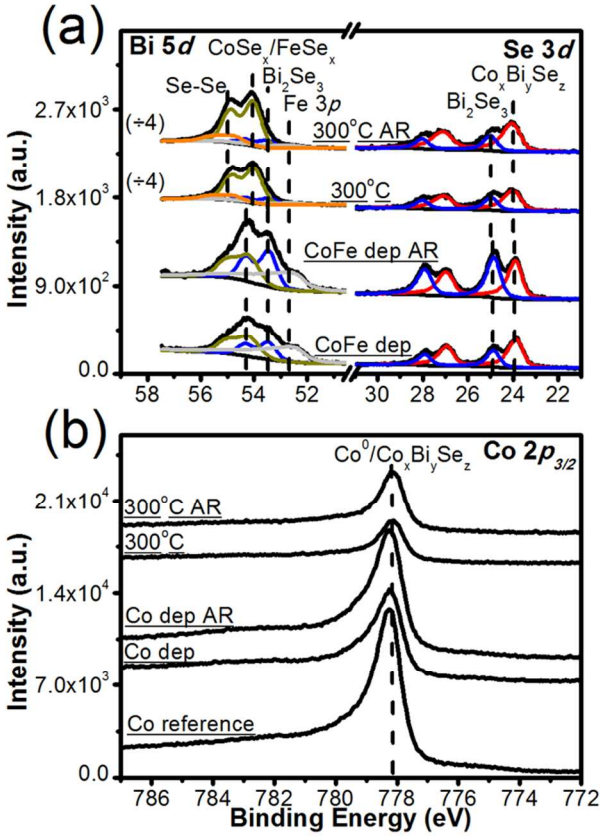

Figure 10: XPS spectra of (a) the Se 3*d* and Bi 5*d* core levels of Bi_2Se_3 after CoFe deposition and following a 300°C anneal. Note the Se 3*d* spectra after annealing have been divided by a factor of 4 for easier comparison. (b) The Co $2p_{3/2}$ core level of a thick Co reference film, Co as-deposited on Bi_2Se_3, and following a 300°C anneal.

Ni – Bi_2Se_3

Ni and permalloy ($Ni_{0.8}Fe_{0.2}$) are some of the primary magnetic materials of interest in TI based spin-transfer torque devices.[3, 54] Ni has been predicted by density functional theory to show significant reaction with other inert materials such as MoS_2,[55] and similar interactions have previously been used to form alloyed source/drain contacts in III-V materials.[56-57] Figure 11a shows the Bi 5*d* and Se 3*d* spectra for a Bi_2Se_3 sample after Ni deposition, along with bulk-sensitive AR spectra. In the Bi 5*d* spectrum, a new peak appears at lower BE after Ni deposition.

This peak is located 0.2 eV higher in BE than expected for Bi^0 as shown in Figure S2c suggesting it may be a $Ni_xBi_ySe_z$ alloy, which has been grown previously with 3% Ni.[58] The Ni/Bi_2Se_3 interface was previously investigated from a band-bending perspective, and a similar lower BE feature was seen in the XPS spectra and identified as metallic Bi, although no metallic Bi spectra were shown by way of comparison, nor any Se core levels.[18] In the Se 3*d* feature we see a peak at higher BE indicative of a Ni-Se interaction. This could be the $Ni_xBi_ySe_z$ alloy observed in the Bi 5*d* or, a Se-rich $NiSe_x$ compound, possibly $NiSe_2$.[51] Ni-chalcogen interaction has previously been reported for Ni deposited on Bi_2Te_3, with $NiTe_2$ formed at the interface and significant interdiffusion.[52] Figure 11b shows the corresponding Ni $2p_{3/2}$ spectra where no significant shift but a slight reduction in the peak asymmetry is observed between a thick (20 nm) Ni reference and Ni on Bi_2Se_3, which is consistent with the $NiSe_x$ detected in the Se 3*d* spectra. The change in lineshape is highlighted in normalized and aligned spectra in Figure S9a.

Our experimental results, along with the simulations by *Spataru et al.* which showed a significant disruption of the Bi_2Se_3 surface states when in contact with Ni,[11] indicate that Ni is not an ideal material to use as a Bi_2Se_3 contact. At a minimum, there must be awareness that the device design must consider the fact that approximately the first 1-2 quintuple layers of Bi_2Se_3 will react with Ni (along with the electronic hybridization) and therefore must be treated as sacrificial layers.

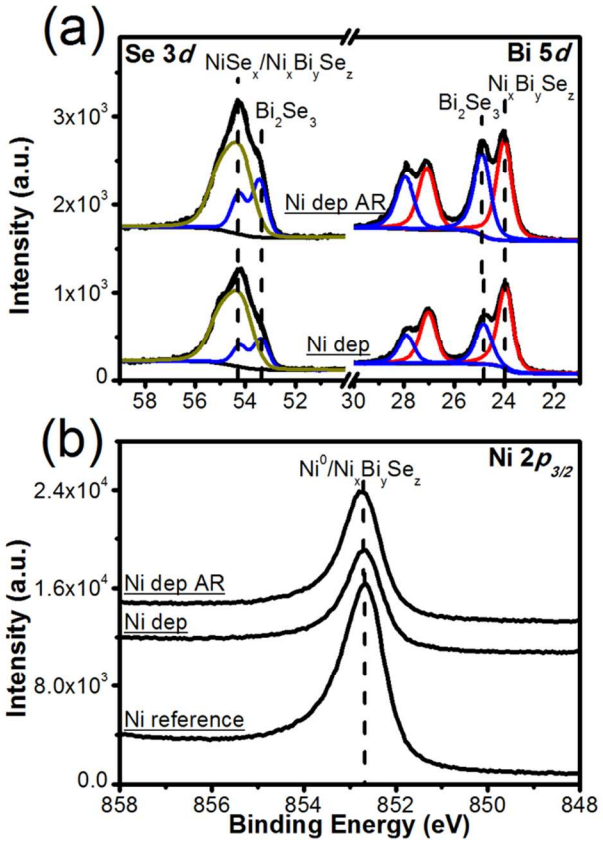

Figure 11: XPS spectra of (a) the Se 3*d* and Bi 5*d* core levels of Bi_2Se_3 after Ni deposition. (b) The Ni $2p_{3/2}$ core level shows no change in lineshape between the Ni reference and Ni on Bi_2Se_3.

$Ni_{0.8}Fe_{0.2} - Bi_2Se_3$

$Ni_{0.8}Fe_{0.2}$ or permalloy (hereafter referred to simply as "NiFe") is the primary ferromagnetic alternative to CoFeB used in the topological insulator based spin-transfer torque literature reported thus far.[3] The actual stoichiometry of the deposited film was determined from XPS fitting of the Ni 2*p* and Fe 3*p* core levels as $Ni_{0.79}Fe_{0.21}$. Figure 12a shows the Bi 5*d* and Se 3*d* core level spectra for NiFe on Bi_2Se_3. Unlike the case of CoFe the reactions observed are not completely dominated by Ni, rather it is a combination with the behavior observed for Fe on Bi_2Se_3. In the Bi 5*d* upon deposition the spectra are dominated by a lower BE peak with a

position identical to that seen in the Ni-only study (Figure S2c), possibly due to a $Ni_xBi_ySe_z$ alloy. The intensity of this peak relative to the Bi_2Se_3 peak is much larger than observed for Ni, indicating the presence of Fe accelerates the reaction. The Se 3*d* spectra is dominated by a feature at 54.1 eV, a nearly identical BE to the previously observed $FeSe_x$ and $NiSe_x$. Although there is likely a mix of the two species, this peak likely comes predominantly from $NiSe_x$ simply due to the amount of Ni in the deposited permalloy. Se-Se bonding is also detected at higher BE, behavior similar to that observed after Fe deposition. Bulk-sensitive AR spectra indicate that both the $Ni_xBi_ySe_z$ and $NiSe_x/FeSe_x$ are surface localized. The formation of this interfacial layer can be seen in Figure 13, where a cross-sectional TEM shows the presence of a 2-3 nm thick interfacial layer between the NiFe and Bi_2Se_3. This is similar to the magnetic dead layer which has been reported for Co films deposited on Bi_2Se_3.[53] The Ni $2p_{3/2}$ spectra (Figure 12b) for NiFe deposited on Bi_2Se_3 is nearly identical to the reference Ni film (Figure S10a) and is identical to the Ni deposited on Bi_2Se_3. Both the Ni and Fe signals decrease to near detection limits after the anneal, likely due to desorption. In both the Fe and CoFe systems we see that Fe is stable on the Bi_2Se_3 at 300°C, indicating that the reason for its loss here is likely due to Ni desorption.

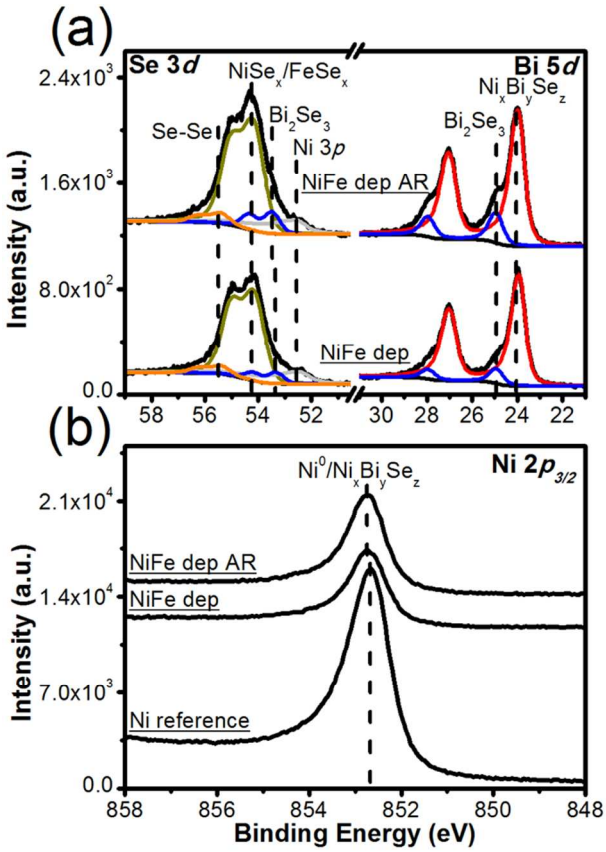

Figure 12: XPS spectra of (a) the Se 3*d* and Bi 5*d* core levels of Bi_2Se_3 after NiFe deposition. (b) The Ni $2p_{3/2}$ core level shows no change in lineshape between the Ni reference and NiFe on Bi_2Se_3.

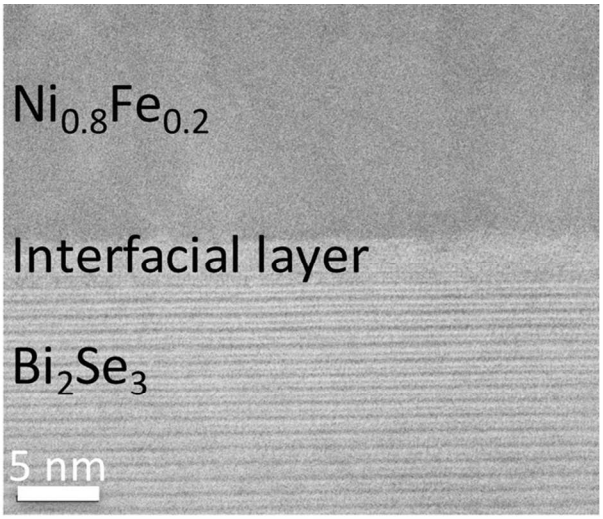

Figure 13: Cross-sectional TEM image of NiFe deposited on Bi_2Se_3. An additional interfacial layer ~3 nm thick can be observed between the two materials.

Discussion

The reactions observed for the contact metals can be grouped together by similarity in the degree of reaction and new species formed.

Au: Au is the sole contact metal for which virtually no interaction with Bi_2Se_3 is observed. A small Bi^0 peak does appear following Au deposition but it is <1% of the detected Bi signal. The Au film then desorbs from the Bi_2Se_3 surface almost completely following 300°C anneal.

Ir and Pd: Ir and Pd exhibit similar behavior to each other, with both materials showing significant reaction with Bi_2Se_3, although the reaction occurs over a relatively shallow depth (~1 nm according to the suppression of the Bi_2Se_3 features). For both, the low BE peak in the Bi 5*d* spectra is at ~0.3 eV higher BE than Bi^0 indicating this peak is due to a different species, likely $Ir_xBi_ySe_z$ and $Pd_xBi_ySe_z$, materials which have been previously investigated as a half metal[40] and a noncentrosymmetric semiconductor,[36] respectively. A higher BE peak is observed in the Se 3*d* consistent with the $Ir_xBi_ySe_z/Pd_xBi_ySe_z$ combined with $IrSe_x/PdSe_x$. One difference is the

thermal stability of the metal layers. Like Au, Pd desorbs almost completely upon anneal, with all spectra reverting to those expected for a bare Bi_2Se_3 surface. However, Ir remains stable following anneal with only a slight increase in the reaction products.

Cr and Fe: This group is more aggressive in their reaction with the underlying Bi_2Se_3. For Cr, the Bi_2Se_3 peak is still reasonably strong following deposition but is attenuated significantly upon anneal. For Fe, the Bi_2Se_3 peak cannot be detected after Fe deposition or the subsequent anneal. Significant Se out-diffusion and conversion of the metal overlayer to a metal-Se_x is observed in the Se 3*d* and metal core levels for both Cr and Fe following anneal. One major difference in the behavior between Cr and Fe is that the Bi 5*d* attenuates significantly following anneal for Cr, while no attenuation is observed for Fe. This may indicate clustering of the Fe/$FeSe_x$.

Co and Ni: Co and Ni exhibit reactions that are a combination of the behaviors observed for the other metals. Upon deposition, they show similar reactivity to Ir or Pd, with the appearance of a $NiSe_x$/$CoSe_x$ in the Se 3*d* and a lower BE peak at ~0.1 eV higher BE than for Bi^0. This peak has been attributed to an interaction between Ni/Co and Bi_2Se_3 resulting in the formation of $Ni_xBi_ySe_z$/$Co_xBi_ySe_z$. While Ni desorbs upon anneal, similar to Ir and Pd, Co remains and reacts further with the Bi_2Se_3, showing Se out-diffusion similar to Cr and Fe, and a dramatic increase in $CoSe_x$. No attenuation of the Bi 5*d* is observed for Co, suggesting similar clustering to that described previously for Fe-only deposition. The Co and Ni $2p_{3/2}$ spectra are identical to those of the reference films, with no peak shift or change in lineshape even after annealing.

CoFe and NiFe: Given the comparable compositions of CoFe and NiFe (80% Ni/Co, 20% Fe), the behavior observed would be expected to be nearly identical to Co or Ni, respectively. This is the case for CoFe, although Fe does play an additional role in the reaction behavior. The BE

position of $FeSe_x$ and $CoSe_x$ are identical (both at 54.2 eV) so there is presumably a mix of the two states present in the Se 3*d*. Se-Se bonding is also detected for CoFe, which is enabled by the presence of Fe, as it is not detected for Co-only. Interestingly, both Co and Fe display behavior potentially explained by clustering, but the alloyed CoFe does not, with the Bi 5*d* showing significant attenuation concurrent with Se out-diffusion.

In the case of NiFe, the Fe seems to have a stronger impact on the interface chemistry. While the behavior is similar to that described for Ni-only, it proceeds more aggressively, with the Bi_2Se_3 feature almost completely attenuated in the Bi 5*d* and Se 3*d*. Se-Se bonding is once again detected, as in CoFe.

Summary

Aside from Au, all other metals show significant interaction with the Bi_2Se_3 upon deposition. The common processing issues with direct Au contacts such as poor adhesion and subsequent delamination mean that although Au provides the most ideal interface it is probably not suitable for device fabrication. In a device with a thick Bi_2Se_3 channel layer, significant chemical reaction between the metal and TI will, according to theory, result in the topologically protected surface states "moving" deeper into the film, away from the reacted interfacial region, to the topmost layer that has not reacted or interacted with the metal.[59] This has been observed experimentally at the interface of surface oxides and TIs, and in TIs with significant surface disorder.[60-61] However, the opposite surface state wavefunction overlap in ultrathin (<6 QL) Bi_2Se_3 films results in the opening of a bandgap in the surface states. As such, significant reaction between metal contacts and the TI in thin film TIs (<~10 QL) will disrupt the topological properties of the surface states by enabling wavefunction overlap through thinning of the unreacted topological insulator. This highlights the fact that the contact/Bi_2Se_3 interaction

(and dielectric/TI interaction) must be accounted for when designing devices, especially in the case of applications with thin Bi_2Se_3 layers.[12, 14, 62]

Figure 14a shows a scatter plot showing the percentage of the Bi 5*d* signal which is attributed to either Bi^0 (in the case of Fe, Cr, and Au) or a Bi intermetallic (in the case of Pd, Ir, Ni, Co, NiFe, and CoFe), as a function of the metal vacuum workfunction. The metal workfunctions are obtained from reported literature values,[63] apart from CoFe which was measured using ultraviolet photoelectron spectroscopy (UPS), as shown in Figure S11. This data is all taken from the as-deposited metal on Bi_2Se_3 data. The Bi^0/intermetallic peak is used as a proxy for the reactivity of the metal/Bi_2Se_3 interface. The reasons for this are 1) the Bi 5*d* peak is not convoluted by overlap with any other peaks, and 2) any reaction between the metal and Bi will show up in this peak, either as residual Bi^0 due to a metal-Se reaction, or as an intermetallic if the Bi directly participates in the formation of an alloy. From this plot, we can see that the low workfunction metals (Fe, Cr, NiFe) demonstrate the strongest interaction. However, significant reaction is observed in almost all cases, with the exception of Au. The strength of the metal-Bi_2Se_3 interaction based upon this plot can be approximately ordered from weakest to strongest as follows: Au < Pd < Ir < Co ≤ CoFe < Ni < Cr < NiFe < Fe. This agrees well with the order of reaction strength as predicted by thermodynamic data shown in Figure 14b, which is: Au^{33} < Pd^{64} < Co^{33} < Ni^{33} < Cr^{45} < Fe.[33] This assumes only metal-Se interactions and uses the values for the metal-Se alloy expected at 300 K, as there is no thermodynamic data for the intermetallic species ($Ni_xBi_ySe_z$, $Co_xBi_ySe_z$, $Pd_xBi_ySe_z$, and $Ir_xBi_ySe_z$). There is no available thermodynamic data for Ir-Se, CoFe-Se, or NiFe-Se interactions so these are not included. Comparing the Gibbs free energies of the metal-Se alloys with that of Bi_2Se_3 it shows that none of Au, Pd, Co, or Ni

are thermodynamically favored to form a metal-Se alloy at room temperature. Interestingly, these are the metals which form the intermetallic species with Bi.

Both plots indicate that Au (and to a lesser degree Pd) is the preferred contact material in minimizing any alloying. CoFe has been omitted from this plot as we do not currently have any measurement or reference for its vacuum workfunction value, but it shows a near-identical reactivity to Co.

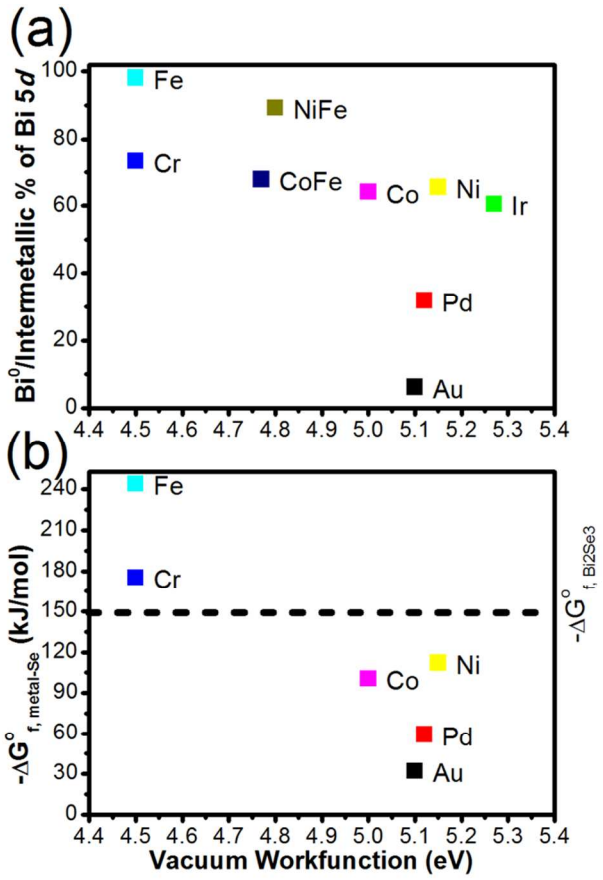

Figure 14: (a) A scatter plot showing the percentage of the Bi 5*d* signal which is attributed to either Bi^0 (in the case of Fe, Cr, and Au) or a Bi intermetallic (in the case of Pd, Ir, Ni, Co, NiFe, and CoFe) as a function of the metal vacuum workfunction. The data is all taken from the as-deposited metal on Bi_2Se_3 spectra. (b) A scatter plot showing the Gibbs free energy for the metal-Se alloy as a function of metal vacuum workfunction. These are: Fe_3Se_4,[33] Cr_2Se_3,[45] $CoSe_2$,[33] $PdSe_2$,[64] AuSe,[33] and $NiSe_2$.[33] The dotted line is $\Delta G^\circ_{f,\ Bi2Se3}$, shown for comparison.

In terms of the ferromagnet/TI structures it appears the best contact choice is Co or CoFe-based (including CoFeB). The amount of Bi_2Se_3 consumed in any reaction between the ferromagnet and TI has additional importance because, along with concern for barriers to charge and spin injection, the presence of a magnetically dead layer at the interface, as has been observed for Co and NiFe on Bi_2Se_3, may limit device efficiency and performance.[53]

Conclusions

The interface chemistry between the topological insulator Bi_2Se_3 and a range of contact metals (Au, Pd, Ir, Cr, Co, Fe, Ni, $Co_{0.8}Fe_{0.2}$, and $Ni_{0.8}Fe_{0.2}$) has been explored. No interfacial layer between metal and Bi_2Se_3 is observed for Au while all others show significant reaction and the formation of metal-selenides, metallic Bi, or intermetallic alloys ($Ir_xBi_ySe_z$, $Pd_xBi_ySe_z$, $Ni_xBi_ySe_z$, and $Co_xBi_ySe_z$). Ferromagnetic materials also exhibit significant reactions and intermixing with the Bi_2Se_3, likely the root of previously reported dead layers at TI/ferromagnet interfaces. These results identify the complexity of metal-Bi_2Se_3 interfaces, and the importance of considering these interactions especially in the use of ultra-thin Bi_2Se_3 layers where they may influence the topologically protected surface states.

Acknowledgements

This work is supported in part by the SWAN Center, a SRC center sponsored in part by the Nanoelectronics Research Initiative and NIST. This work was also supported in part by NSF Award No. 1407765 under the US/Ireland UNITE collaboration. This work has also received funding in part from the European Union's Horizon 2020 research and innovation program under the Marie Skłodowska-Curie grant agreement No 713567 and a research grant from Science Foundation Ireland (SFI) under Grant Number SFI/12/RC/2278.

Supporting Information Available

Additional Bi 5*d*, Se 3*d*, and metal core level XPS spectra for all of the metals deposited on Bi_2Se_3; Comparative Bi 5*d* spectra of metallic Bismuth and the metals deposited on Bi_2Se_3;

Scatter plots showing the total area of each core level peak as a function of experimental step; UPS spectra for Au, Ni, and $Co_{0.8}Fe_{0.2}$. This information is available free of charge via the Internet at http://pubs.acs.org

References

1. Moore, J. Topological Insulators: The Next Generation. *Nat. Phys.* **2009**, *5*, 378-380.

2. Moore, J. E. The Birth of Topological Insulators. *Nature* **2010**, *464*, 194-198.

3. Mellnik, A. R.; Lee, J. S.; Richardella, A.; Grab, J. L.; Mintun, P. J.; Fischer, M. H.; Vaezi, A.; Manchon, A.; Kim, E. A.; Samarth, N., et al. Spin-Transfer Torque Generated by a Topological Insulator. *Nature* **2014**, *511*, 449-451.

4. Lu, H.; Seabaugh, A. Tunnel Field-Effect Transistors: State-of-the-Art. *IEEE J. Electron Devices Soc.* **2014**, *2*, 44-49.

5. Vandenberghe, W. G.; Fischetti, M. V. Imperfect Two-Dimensional Topological Insulator Field-Effect Transistors. *Nat. Commun.* **2017**, *8*, 14184.

6. Zhang, Y.; He, K.; Chang, C. Z.; Song, C. L.; Wang, L. L.; Chen, X.; Jia, J. F.; Fang, Z.; Dai, X.; Shan, W. Y., et al. Crossover of the Three-Dimensional Topological Insulator Bi_2Se_3 to the Two-Dimensional Limit. *Nat. Phys.* **2010**, *6*, 584-588.

7. Tsipas, P.; Xenogiannopoulou, E.; Kassavetis, S.; Tsoutsou, D.; Golias, E.; Bazioti, C.; Dimitrakopulos, G. P.; Komninou, P.; Liang, H.; Caymax, M., et al. Observation of Surface Dirac Cone in High-Quality Ultrathin Epitaxial Bi_2Se_3 Topological Insulator on AlN (0001) Dielectric. *ACS Nano* **2014**, *8*, 6614-6619.

8. Chen, Z.; Zhao, L.; Park, K.; Garcia, T. A.; Tamargo, M. C.; Krusin-Elbaum, L. Robust Topological Interfaces and Charge Transfer in Epitaxial Bi_2Se_3/II–VI Semiconductor Superlattices. *Nano Lett.* **2015**, *15*, 6365-6370.

9. Taskin, A. A.; Sasaki, S.; Segawa, K.; Ando, Y. Achieving Surface Quantum Oscillations in Topological Insulator Thin Films of Bi_2Se_3. *Adv. Mater.* **2012**, *24*, 5581-5585.

10. Walsh, L. A.; Hinkle, C. L. Van Der Waals Epitaxy: 2D Materials and Topological Insulators (in press). *Appl. Mater. Today* **2017**.

11. Spataru, C. D.; Leonard, F. Fermi-Level Pinning, Charge Transfer, and Relaxation of Spin-Momentum Locking at Metal Contacts to Topological Insulators. *Phys. Rev. B* **2014**, *90*, 085115.

12. Lang, M.; He, L.; Xiu, F.; Yu, X.; Tang, J.; Wang, Y.; Kou, X.; Jiang, W.; Federov, A. V.; Wang, K. L. Revelation of Topological Surface States in Bi_2Se_3 Thin Films by in Situ Al Passivation. *ACS Nano* **2011**, *6*, 295-302.

13. Xu, S.; Han, Y.; Chen, X.; Wu, Z.; Wang, L.; Han, T.; Ye, W.; Lu, H.; Long, G.; Wu, Y., et al. Van Der Waals Epitaxial Growth of Atomically Thin Bi_2Se_3 and Thickness-Dependent Topological Phase Transition. *Nano Lett.* **2015**, *15*, 2645-2651.

14. Cho, S.; Butch, N. P.; Paglione, J.; Fuhrer, M. S. Insulating Behavior in Ultrathin Bismuth Selenide Field Effect Transistors. *Nano Lett.* **2011**, *11*, 1925-1927.

15. Yeh, Y. C.; Ho, P. H.; Wen, C. Y.; Shu, G. J.; Sankar, R.; Chou, F. C.; Chen, C. W. Growth of the Bi_2Se_3 Surface Oxide for Metal–Semiconductor–Metal Device Applications. *J. Phys. Chem. C* **2016**, *120*, 3314-3318.

16. Wang, Y.; Deorani, P.; Banerjee, K.; Koirala, N.; Brahlek, M.; Oh, S.; Yang, H. Topological Surface States Originated Spin-Orbit Torques in Bi_2Se_3. *Phys. Rev. Lett.* **2015**, *114*, 257202.

17. de Jong, N.; Frantzeskakis, E.; Zwartsenberg, B.; Huang, Y. K.; Wu, D.; Hlawenka, P.; Sańchez-Barriga, J.; Varykhalov, A.; van Heumen, E.; Golden, M. S. Angle-Resolved and Core-Level Photoemission Study of Interfacing the Topological Insulator $Bi_{1.5}Sb_{0.5}Te_{1.7}se_{1.3}$ with Ag, Nb, and Fe. *Phys. Rev. B* **2015**, *92*, 075127.

18. Ye, W.; Pakhomov, A. B.; Xu, S.; Lu, H.; Wu, Z.; Han, Y.; Han, T.; Wu, Y.; Long, G.; Lin, J., et al. Band Bending at Interfaces between Topological Insulator Bi_2Se_3 and Transition Metals. *arXiv:1511.03421* **2015**.

19. University Wafer. http://www.universitywafer.com/.

20. Walsh, L. A.; Yue, R.; Wang, Q.; Barton, A. T.; Addou, R.; Smyth, C. M.; Zhu, H.; Kim, J.; Colombo, L.; Kim, M. J., et al. WTe_2 Thin Films Grown by Beam-Interrupted Molecular Beam Epitaxy. *2D Mat.* **2017**, *4*, 025044.

21. Wallace, R. M. In-Situ Studies of Interfacial Bonding of High-k Dielectrics for CMOS Beyond 22nm. *ECS Trans.* **2008**, *16*, 255-271.

22. Smyth, C. M.; Addou, R.; McDonnell, S.; Hinkle, C. L.; Wallace, R. M. Contact Metal-MoS_2 Interfacial Reactions and Potential Implications on MoS_2-Based Device Performance. *J. Phys. Chem. C* **2016**, *120*, 14719-14729.

23. International, A. ASTM E2108 - 10 Standard Practice for Calibration of the Electron Binding-Energy Scale of an X-Ray Photoelectron Spectrometer. 2000.

24. Wagner, C. D.; Davis, L. E.; Zeller, M. V.; Taylor, J. A.; Raymond, R. H.; Gale, L. H. Empirical Atomic Sensitivity Factors for Quantitative-Analysis by Electron-Spectroscopy for Chemical-Analysis. *Surf. Interface Anal.* **1981**, *3*, 211-225.

25. Herrera-Gomez, A.; Hegedus, A.; Meissner, P. L. Chemical Depth Profile of Ultrathin Nitrided SiO_2 Films. *Appl. Phys. Lett.* **2002** *81*, 1014-1016.

26. Eddrief, M.; Atkinson, P.; Etgens, V.; Jusserand, B. Low-Temperature Raman Fingerprints for Few-Quintuple Layer Topological Insulator Bi_2Se_3 Films Epitaxied on GaAs. *Nanotechnology* **2014**, *25*, 245701.

27. Green, A. J.; Dey, S.; An, Y. Q.; O'Brien, B.; O'Mullane, S.; Thiel, B.; Diebold, A. C. Surface Oxidation of the Topological Insulator Bi_2Se_3. *J. Vac. Sci. Technol. A* **2016**, *34*, 061403.

28. Chen, C.; He, S.; Weng, H.; Zhang, W.; Zhao, L.; Liu, H.; Jia, X.; Mou, D.; Liu, S.; He, J., et al. Robustness of Topological Order and Formation of Quantum Well States in Topological Insulators Exposed to Ambient Environment. *Proc. Natl. Acad. Sci. U.S.A.* **2012**, *109*, 3694-3698.

29. Dai, J. X.; Wang, W. B.; Brahlek, M.; Koirala, N.; Salehi, M.; Oh, S.; Wu, W. D. Restoring Pristine Bi_2Se_3 Surfaces with an Effective Se Decapping Process. *Nano Research* **2015**, *8*, 1222-1228.

30. Moulder, J. F. *Handbook of X-Ray Photoelectron Spectroscopy: A Reference Book of Standard Spectra for Identification and Interpretation of XPS Data* Physical Electronics: Eden Prairie, MN, 1995.

31. Smyth, C. M.; Addou, R.; McDonnell, S.; Hinkle, C. L.; Wallace, R. M. WSe_2-Contact Metal Interface Chemistry and Band Alignment under High Vacuum and Ultra High Vacuum Deposition Conditions. *2D Mat.* **2017**, *4*, 025084.

32. Lee, H. D.; Xu, C.; Shubeita, S. M.; Brahlek, M.; Koirala, N.; Oh, S.; Gustafsson, T. Indium and Bismuth Interdiffusion and Its Influence on the Mobility in In_2Se_3/Bi_2Se_3. *Thin Solid Films* **2014**, *556*, 322-324.

33. Olin, Å.; Noläng, B.; Öhman, L. O.; Osadchii, E.; Rosén, E. *Chemical Thermodynamics of Selenium*; Elsevier Science: Amsterdam, 2005; Vol. 7.

34. Mlack, J. T.; Rahman, A.; Danda, G.; Drichko, N.; Friedensen, S.; Drndić, M.; Marković, N. Patterning Superconductivity in a Topological Insulator. *ACS Nano* **2017**, *11*, 5873-5878.

35. Zhang, G.; Qin, H.; Chen, J.; He, X.; Lu, L.; Li, Y.; Wu, K. Growth of Topological Insulator Bi_2Se_3 Thin Films on $SrTiO_3$ with Large Tunability in Chemical Potential. *Adv. Funct. Mater.* **2011**, *21*, 2351-2355.

36. Joshi, B.; Thamizhavel, A.; Ramakrishnan, S. Superconductivity in Cubic Noncentrosymmetric PdBiSe Crystal. *J. Phys. Conf. Ser.* **2015**, *592*, 012069.

37. Haynes, W. M. *Crc Handbook of Chemistry and Physics*; CRC Press, 2016.

38. Hufner, S.; Wertheim, G. K. Core-Line Asymmetries in X-Ray-Photoemission Spectra of Metals. *Phys. Rev. B* **1975**, *11*, 678.

39. Pu, X. Y.; Zhao, K.; Liu, Y.; Wei, Z. T.; Jin, R.; Yang, X. S.; Zhao, Y. Structural and Transport Properties of Iridium-Doped Bi_2Se_3 Topological Insulator Crystals. *J. Alloys Compd.* **2017**, *694*, 272-275.

40. Liu, Z.; Thirupathaiah, S.; Yaresko, A.; Kushwaha, S.; Gibson, Q.; Cava, R.; Borisenko, S. Non-Magnetic Half-Metals. *arXiv:1705.07431* **2017**.

41. Kim, D.; Cho, S.; Butch, N. P.; Syers, P.; Kirshenbaum, K.; Adam, S.; Paglione, J.; Fuhrer, M. S. Surface Conduction of Topological Dirac Electrons in Bulk Insulating Bi_2Se_3. *Nat. Phys.* **2012**, *8*, 459-463.

42. Hong, S. S.; Cha, J. J.; Kong, D.; Cui, Y. Ultra-Low Carrier Concentration and Surface-Dominant Transport in Antimony-Doped Bi_2Se_3 Topological Insulator Nanoribbons. *Nat. Commun.* **2011**, *3*, 757.

43. Liu, W.; West, D.; He, L.; Xu, Y.; Liu, J.; Wang, K.; Wang, Y.; van der Laan, G.; Zhang, R.; Zhang, S., et al. Atomic-Scale Magnetism of Cr-Doped Bi_2Se_3 Thin Film Topological Insulators. *ACS Nano* **2015**, *9*, 10237-10243.

44. Kresse, G.; Hafner, J. Ab Initio Molecular Dynamics for Liquid Metals. *Phys. Rev. B* **1993**, *47*, 558.

45. Mohanty, B. C.; Malar, P.; Osipowicz, T.; Murty, B. S.; Varma, S.; Kasiviswanathan, S. Characterization of Silver Selenide Thin Films Grown on Cr-Covered Si Substrates. *Surf. Interface Anal.* **2009**, *41*, 170-178.

46. Chen, Y. L.; Chu, J. H.; Analytis, J. G.; Liu, Z. K.; Igarashi, K.; Kuo, H. H.; Qi, X. L.; Mo, S. K.; Moore, R. G.; Lu, D. H., et al. Massive Dirac Fermion on the Surface of a Magnetically Doped Topological Insulator. *Science* **2010**, *329*, 659-662.

47. Majumder, S.; Jarvis, K.; Banerjee, S. K.; Kavanagh, K. L. Interfacial Reactions at Fe/Topological Insulator Spin Contacts. *J. Vac. Sci. Technol. B* **2017**, *35*, 04F105.

48. Scholz, M. R.; Sanchez-Barriga, J.; Marchenko, D.; Varykhalov, A.; Volykhov, A.; Yashina, L. V.; Rader, O. Tolerance of Topological Surface States Towards Magnetic Moments: Fe on Bi_2Se_3. *Phys. Rev. Lett.* **2012**, *108*, 256810.

49. Irfan, B.; Chatterjee, R. Magneto-Transport and Kondo Effect in Cobalt Doped Bi_2Se_3 Topological Insulators. *Appl. Phys. Lett.* **2015**, *107*, 173108.

50. Jamali, M.; Lee, J. S.; Jeong, J. S.; Mahfouzi, F.; Lv, Y.; Zhao, Z. Y.; Nikolic, B. K.; Mkhoyan, K. A.; Samarth, N.; Wang, J. P. Giant Spin Pumping and Inverse Spin Hall Effect in

the Presence of Surface and Bulk Spin-Orbit Coupling of Topological Insulator Bi_2Se_3. *Nano Lett.* **2015**, *15*, 7126-7132.

51. Kwak, I. H.; Im, H. S.; Jang, D. M.; Kim, Y. W.; Park, K.; Lim, Y. R.; Cha, E. H.; Park, J. $CoSe_2$ and $NiSe_2$ Nanocrystals as Superior Bifunctional Catalysts for Electrochemical and Photoelectrochemical Water Splitting. *ACS Appl. Mat. Interfaces* **2016**, *8*, 5327-5334.

52. Gupta, R. P.; Iyore, O. D.; Xiong, K.; White, J. B.; Cho, K.; Alshareef, H. N.; Gnade, B. E. Interface Characterization of Cobalt Contacts on Bismuth Selenium Telluride for Thermoelectric Devices. *Electrochem. Solid-State Lett.* **2009**, *12*, H395-H397.

53. Li, J.; Wang, Z. Y.; Tan, A.; Glans, P. A.; Arenholz, E.; Hwang, C.; Shi, J.; Qiu, Z. Q. Magnetic Dead Layer at the Interface between a Co Film and the Topological Insulator Bi_2Se_3. *Phys. Rev. B* **2012**, *86*, 054430.

54. Yoo, T.; Nasir, A. R.; Bac, S. K.; Lee, S.; Choi, S.; Lee, S.; X. Liu; J. K. Furdyna Magnetic Properties of Ni Films Deposited on MBE Grown Bi_2Se_3 Layers. *AIP Adv.* **2017**, *7*, 055819.

55. Min, K. A.; Cha, J.; Cho, K.; Hong, S. Ferromagnetic Contact between Ni and MoX_2 (X = S, Se, or Te) with Fermi-Level Pinning. *2D Mat.* **2017**, *4*, 024006.

56. Walsh, L. A.; Hughes, G.; Weiland, C.; Woicik, J. C.; Lee, R. T. P.; Loh, W. Y.; Lysaght, P.; Hobbs, C. Ni-(In,Ga)As Alloy Formation Investigated by Hard-X-Ray Photoelectron Spectroscopy and X-Ray Absorption Spectroscopy. *Phys. Rev. Appl.* **2014**, *2*, 064010.

57. Oxland, R.; Chang, S. W.; Li, X.; Wang, S. W.; Radhakrishnan, G.; Priyantha, W.; van Dal, M. J. H.; Hsieh, C. H.; Vellianitis, G.; Doornbos, G., et al. An Ultralow-Resistance Ulltrashallow Metallic Source/Drain Contact Scheme for III-V NMOS. *IEEE Electron Device Lett.* **2012**, *33*, 501-503.

58. Yang, H.; Liu, L. G.; Zhang, M.; Yang, X. S. Growth and Magnetic Properties of Ni-Doped Bi_2Se_3 Topological Insulator Crystals. *Solid State Commun.* **2016**, *241*, 26-31.

59. Schubert, G.; Fehske, H.; Fritz, L.; Vojta, M. Fate of Topological-Insulator Surface States under Strong Disorder. *Phys. Rev. B* **2012**, *85*, 201105.

60. Kong, D.; Cha, J. J.; Lai, K.; Peng, H.; Analytis, J. G.; Meister, S.; Chen, Y.; Zhang, H. J.; Fisher, I. R.; Shen, Z. X., et al. Rapid Surface Oxidation as a Source of Surface Degradation Factor for Bi_2Se_3. *ACS Nano* **2011**, *5*, 4698-4703.

61. Queiroz, R.; Landolt, G.; Muff, S.; Slomski, B.; Schmitt, T.; Strocov, V. N.; Mi, J. L.; Iversen, B. B.; Hofmann, P.; Osterwalder, J., et al. Sputtering-Induced Reemergence of the Topological Surface State in Bi_2Se_3. *Phys. Rev. B* **2016**, *93*, 165409.

62. Bansal, N.; Kim, Y. S.; Brahlek, M.; Edrey, E.; Oh, S. Thickness-Independent Transport Channels in Topological Insulator Bi_2Se_3 Thin Films. . *Phys. Rev. Lett.* **2012**, *109*, 116804.

63. Michaelson, H. B. The Work Function of the Elements and Its Periodicity. *J. Appl. Phys.* **1977**, *48*, 4729-4733.

64. Karzhavin, V. K. Sulfides, Selenides, and Tellurides of Platinum and Palladium: Estimation of Thermodynamic Properties. *Geochem. Int.* **2007**, *45*, 931-937.

TOC graphic

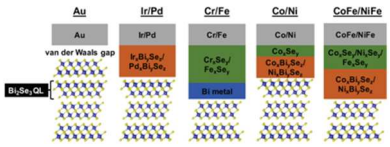
Au
Ir/Pd
Cr/Fe
Co/Ni
CoFe/NiFe
Au
Ir/Pd
Cr/Fe
Co/Ni
CoFe/NiFe
van der Waals gap
Bi metal
Bi2Se3 QL

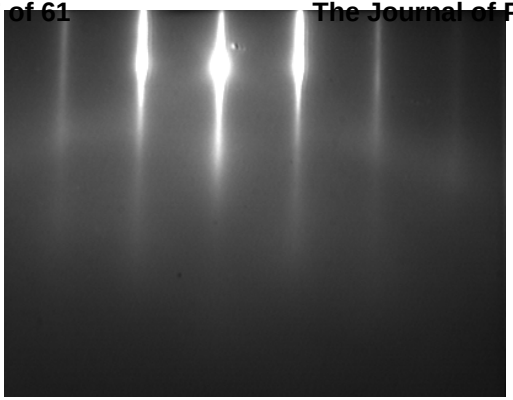

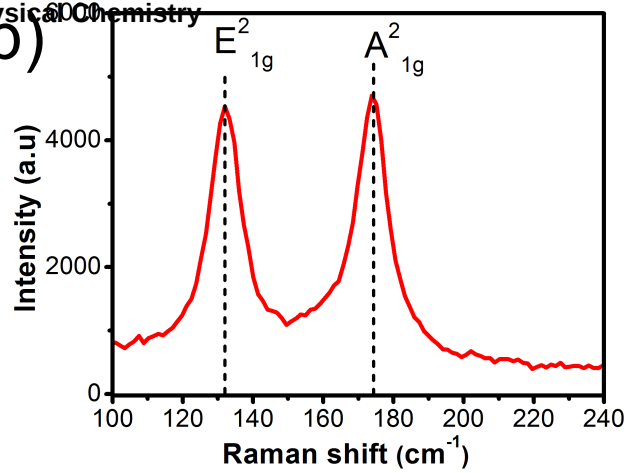

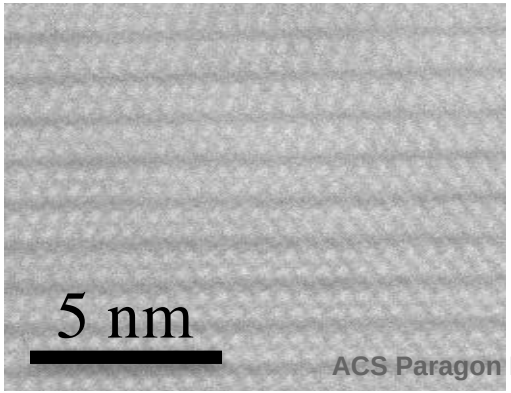

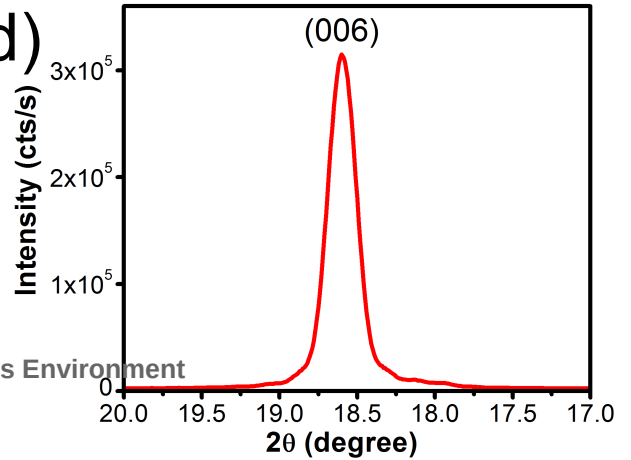

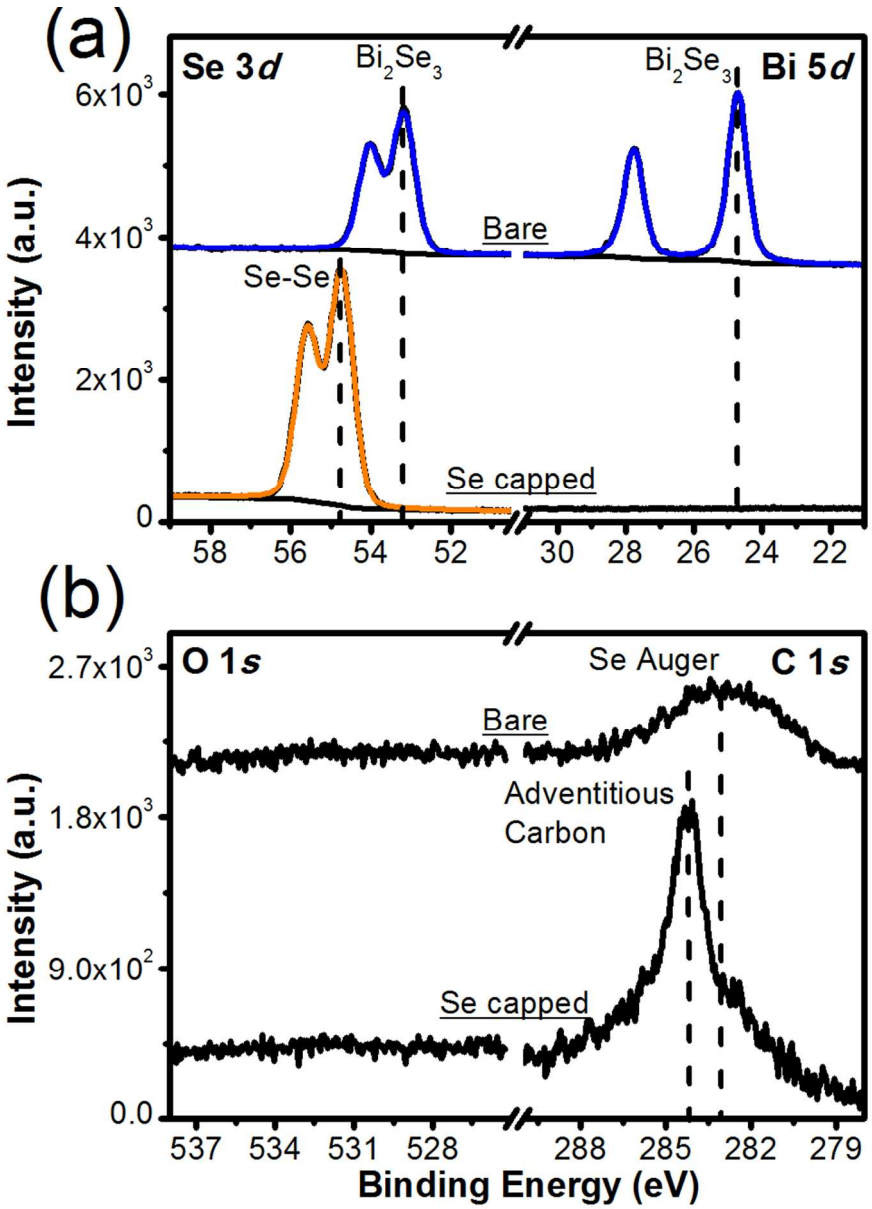

Figure 2

81x112mm (300 x 300 DPI)

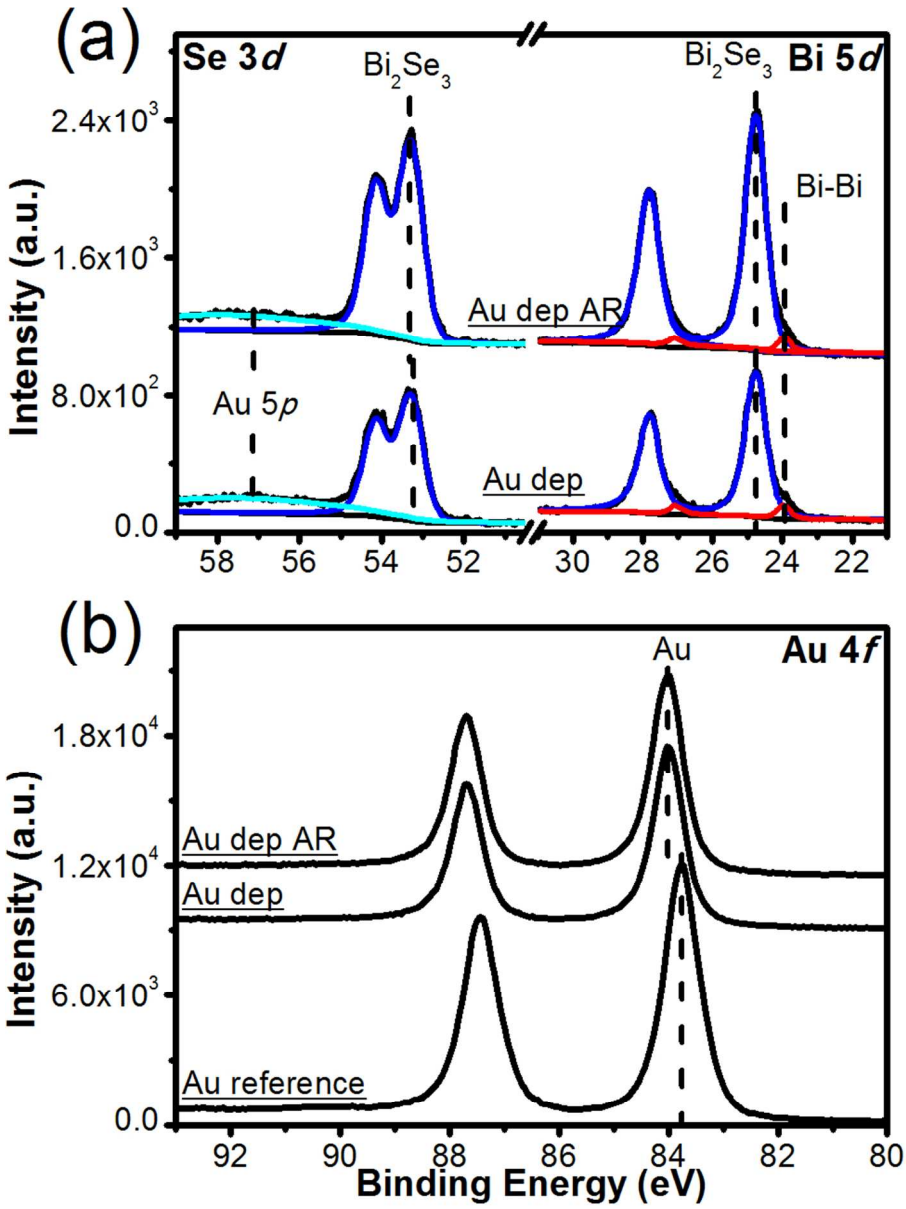

Figure 3

82x109mm (300 x 300 DPI)

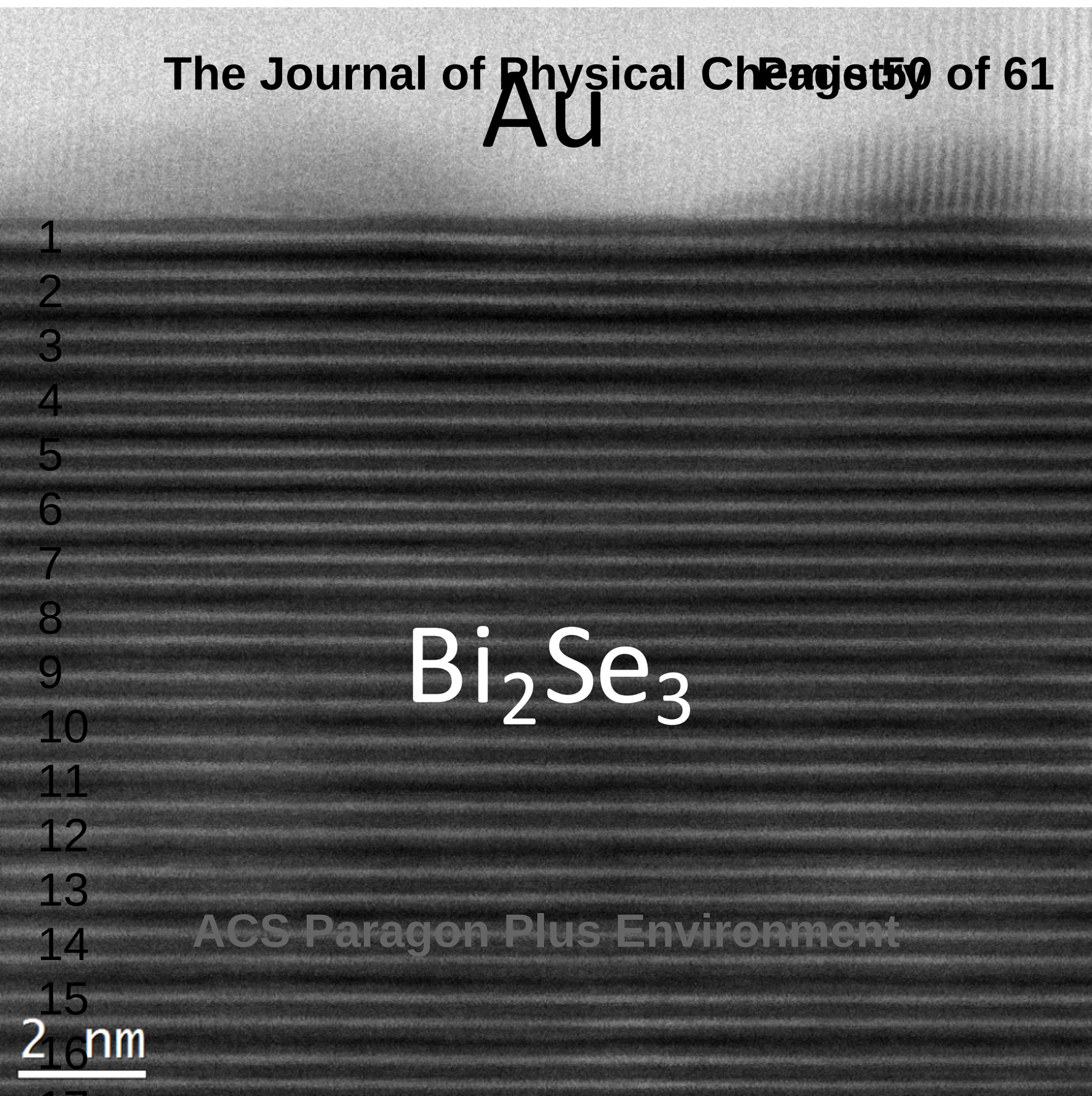
Au
Bi2Se3
ACS Paragon Plus Environment
2 nm

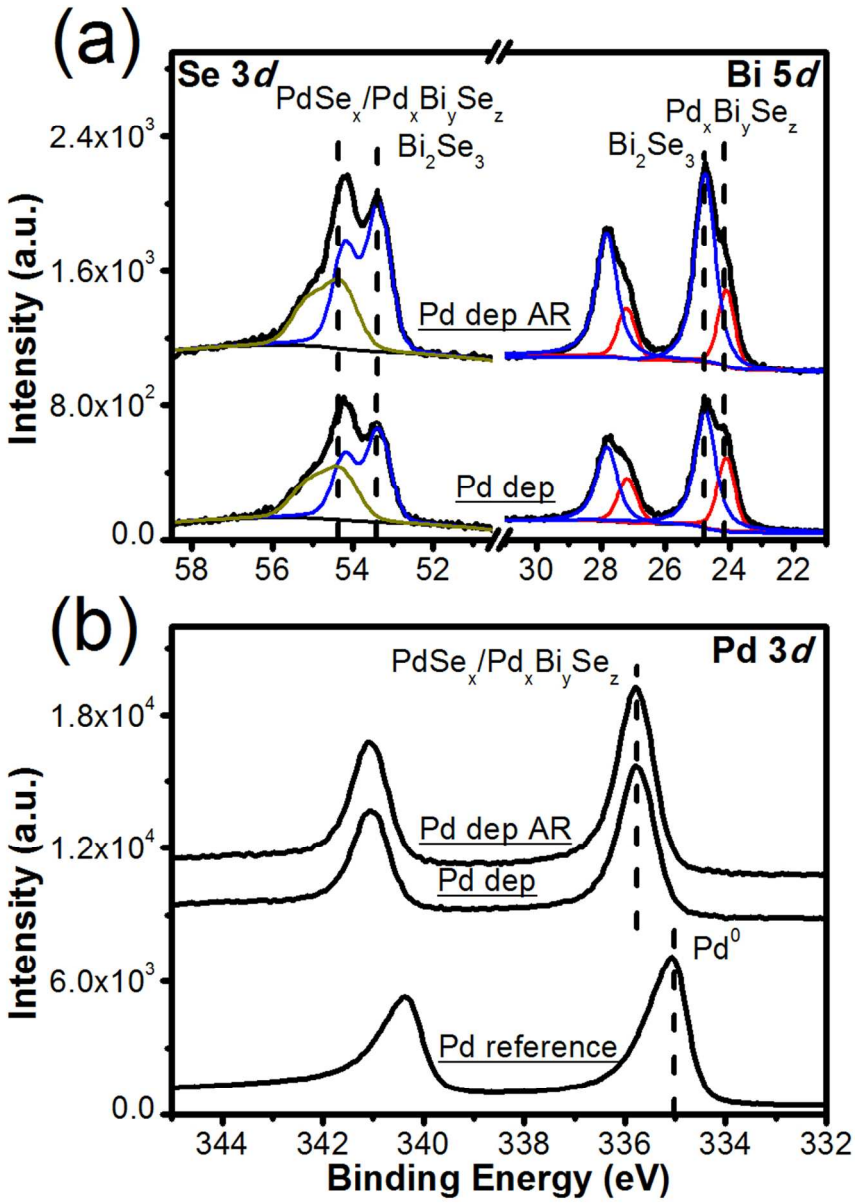

Figure 5

80x111mm (300 x 300 DPI)

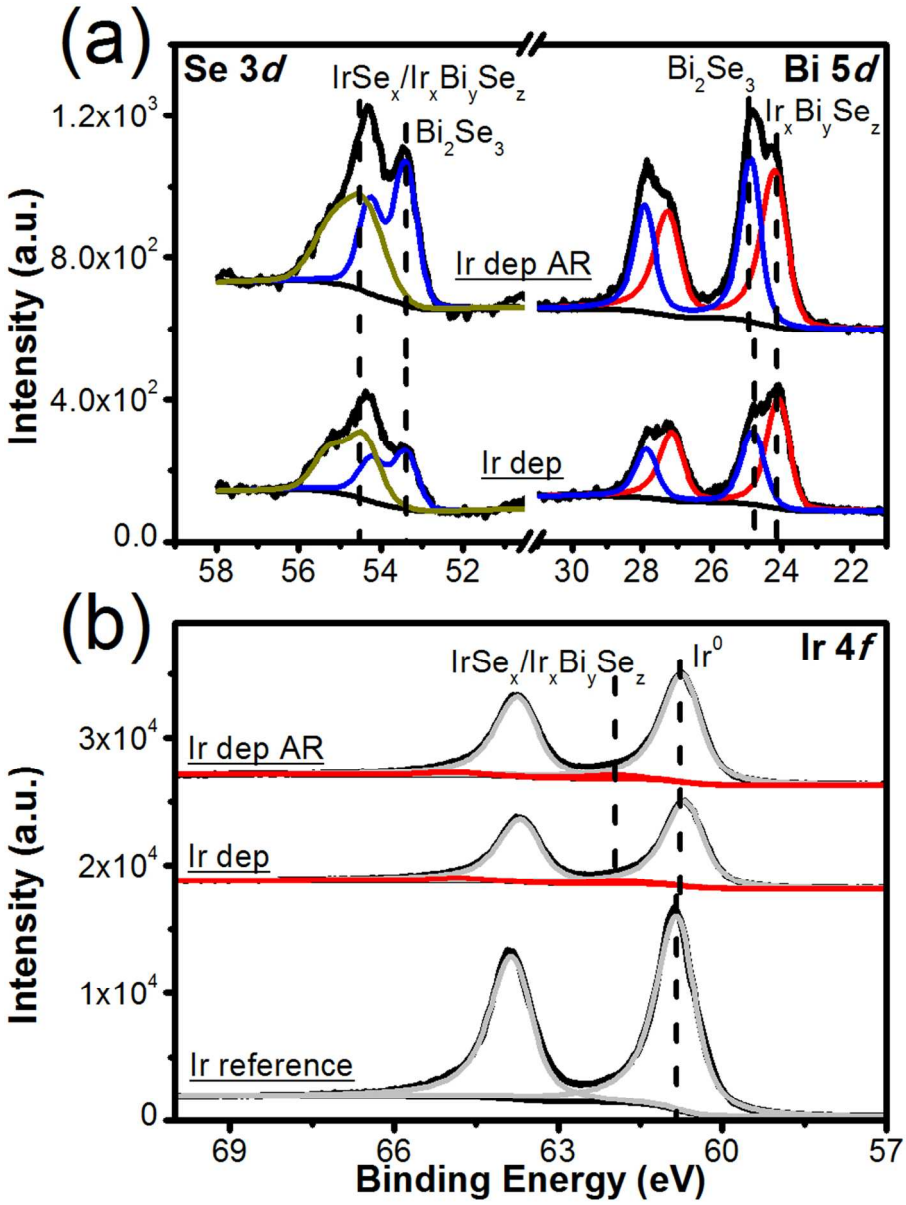

Figure 6

82x109mm (300 x 300 DPI)

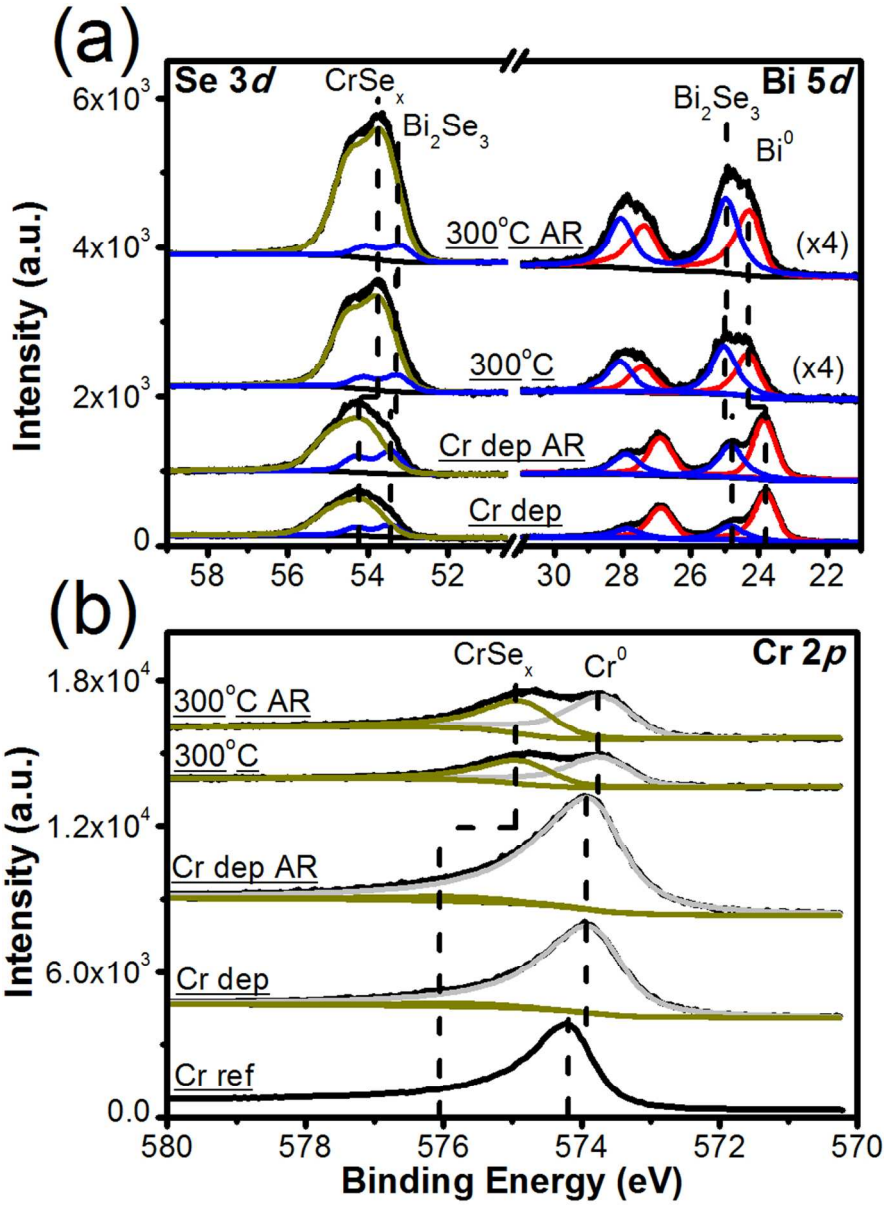

Figure 7

82x112mm (300 x 300 DPI)

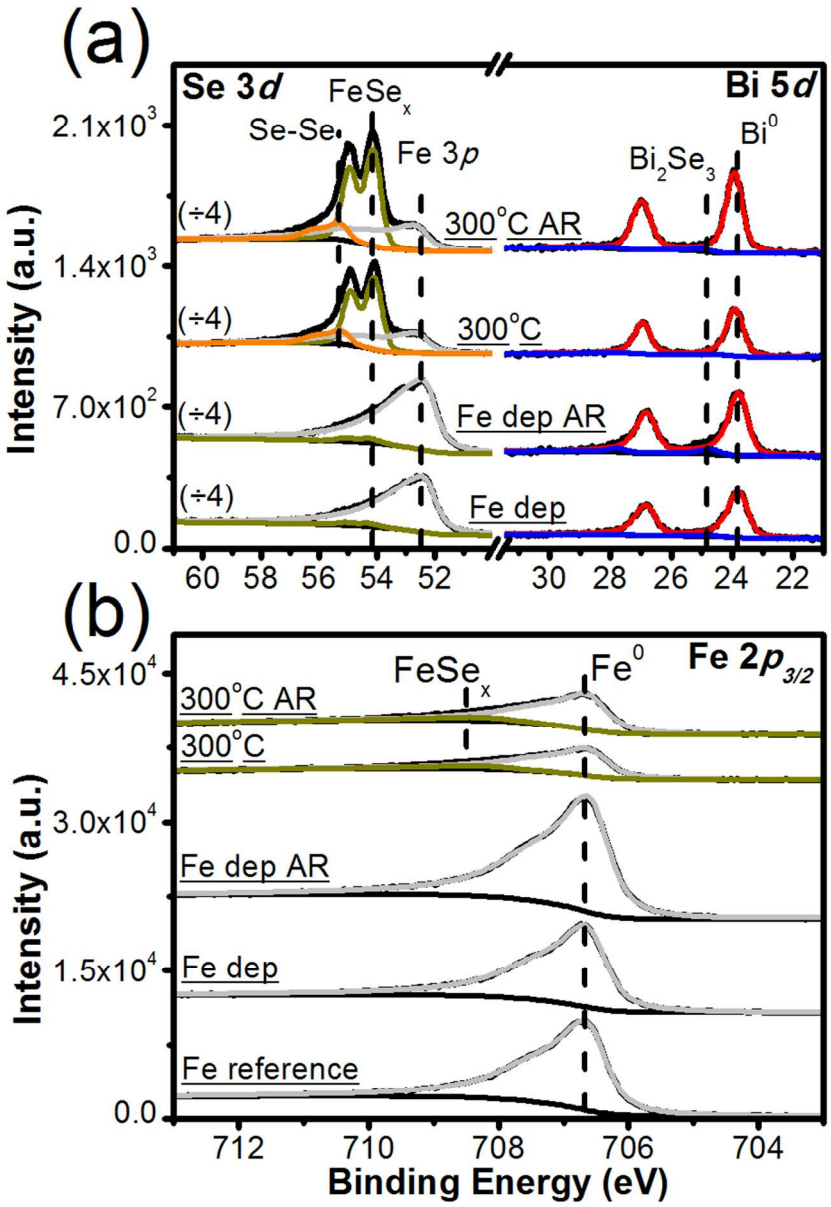

Figure 8

80x112mm (300 x 300 DPI)

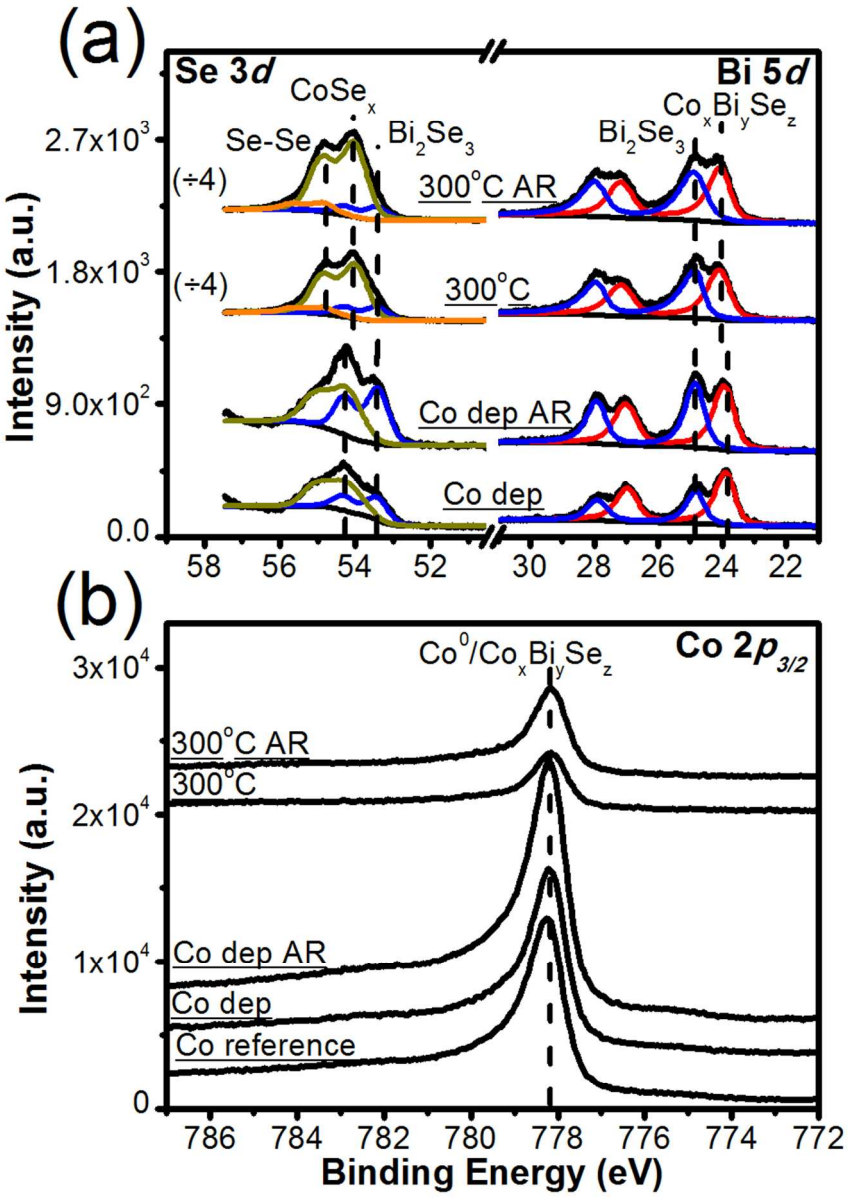

Figure 9

81x112mm (300 x 300 DPI)

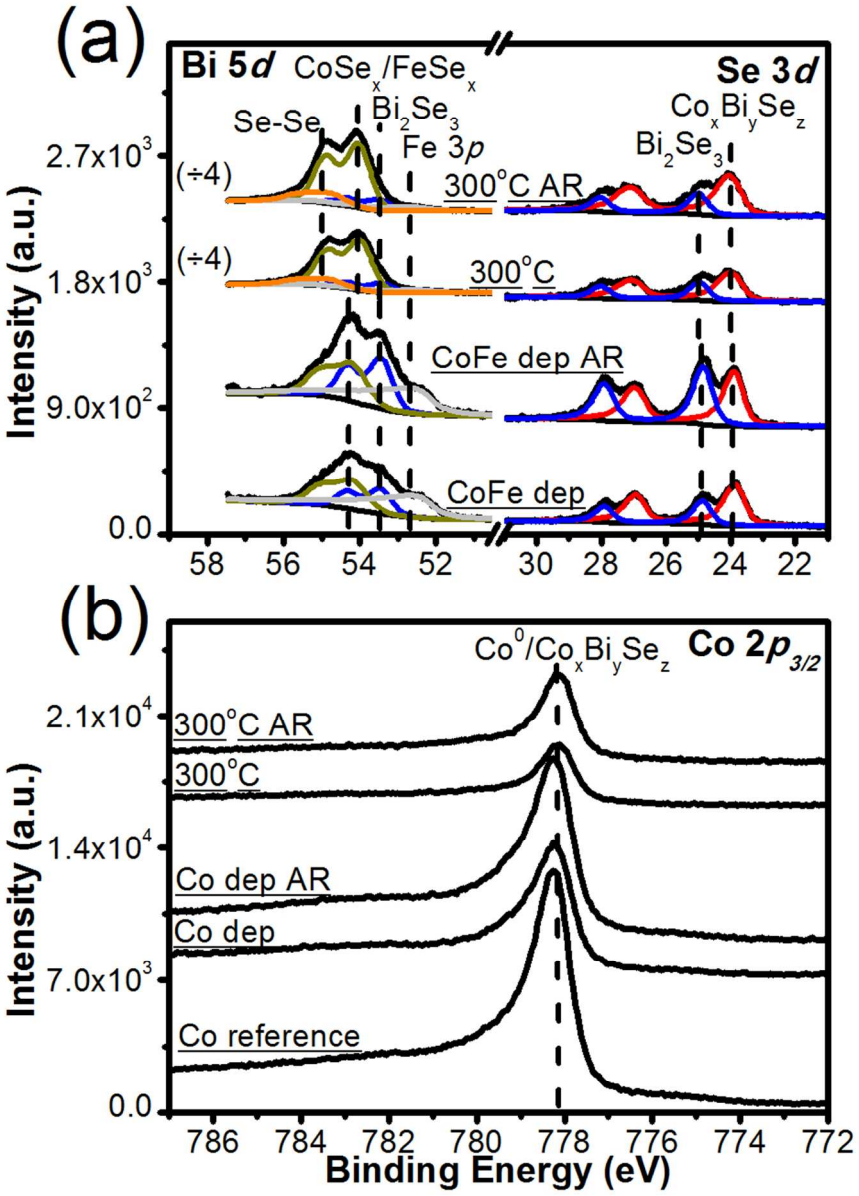

Figure 10

82x110mm (300 x 300 DPI)

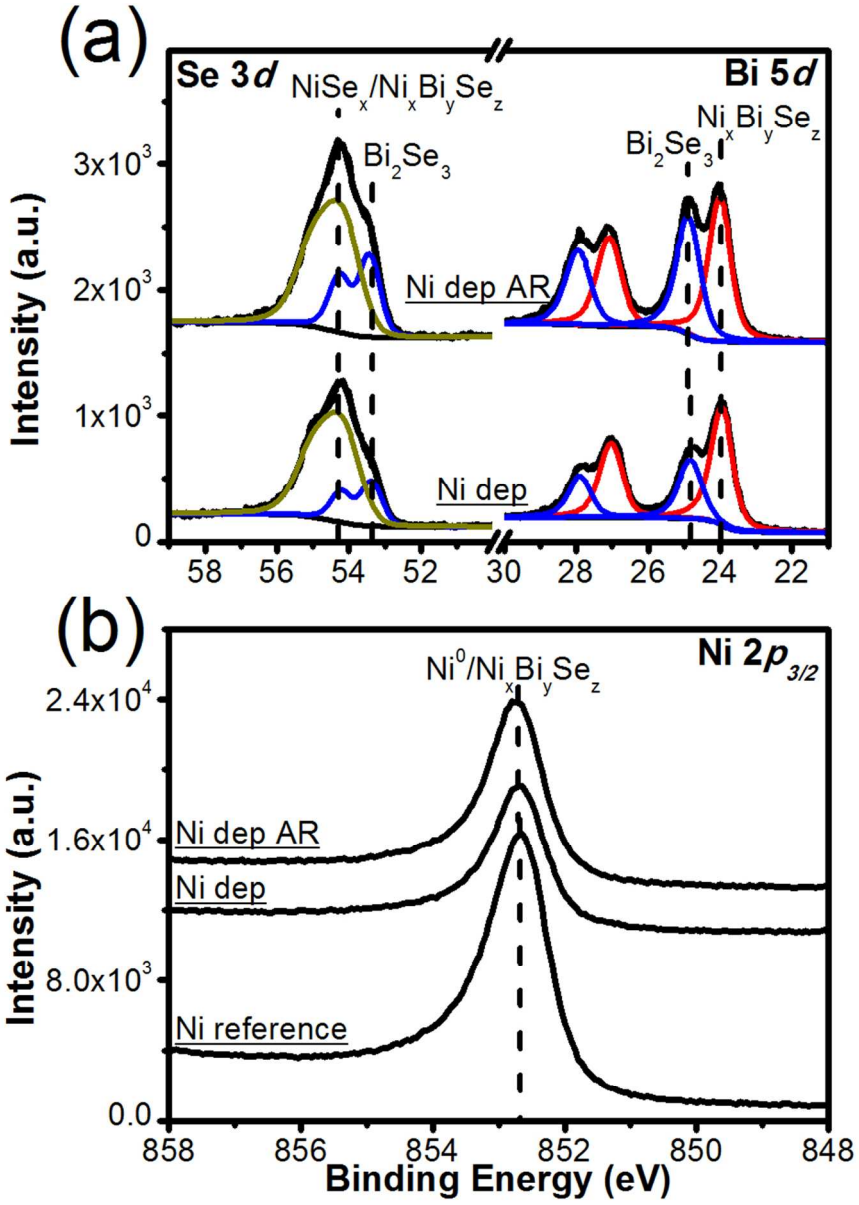

Figure 11

80x110mm (300 x 300 DPI)

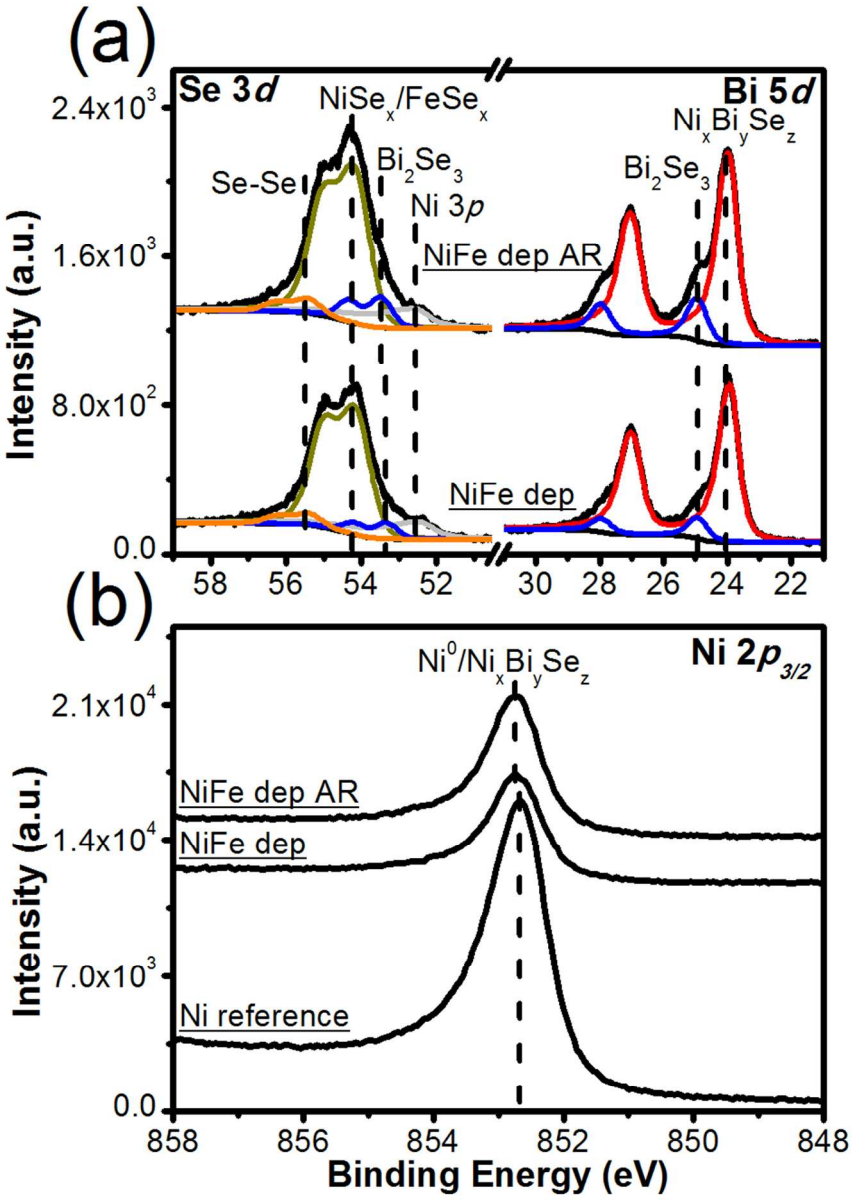

Figure 12

80x112mm (300 x 300 DPI)

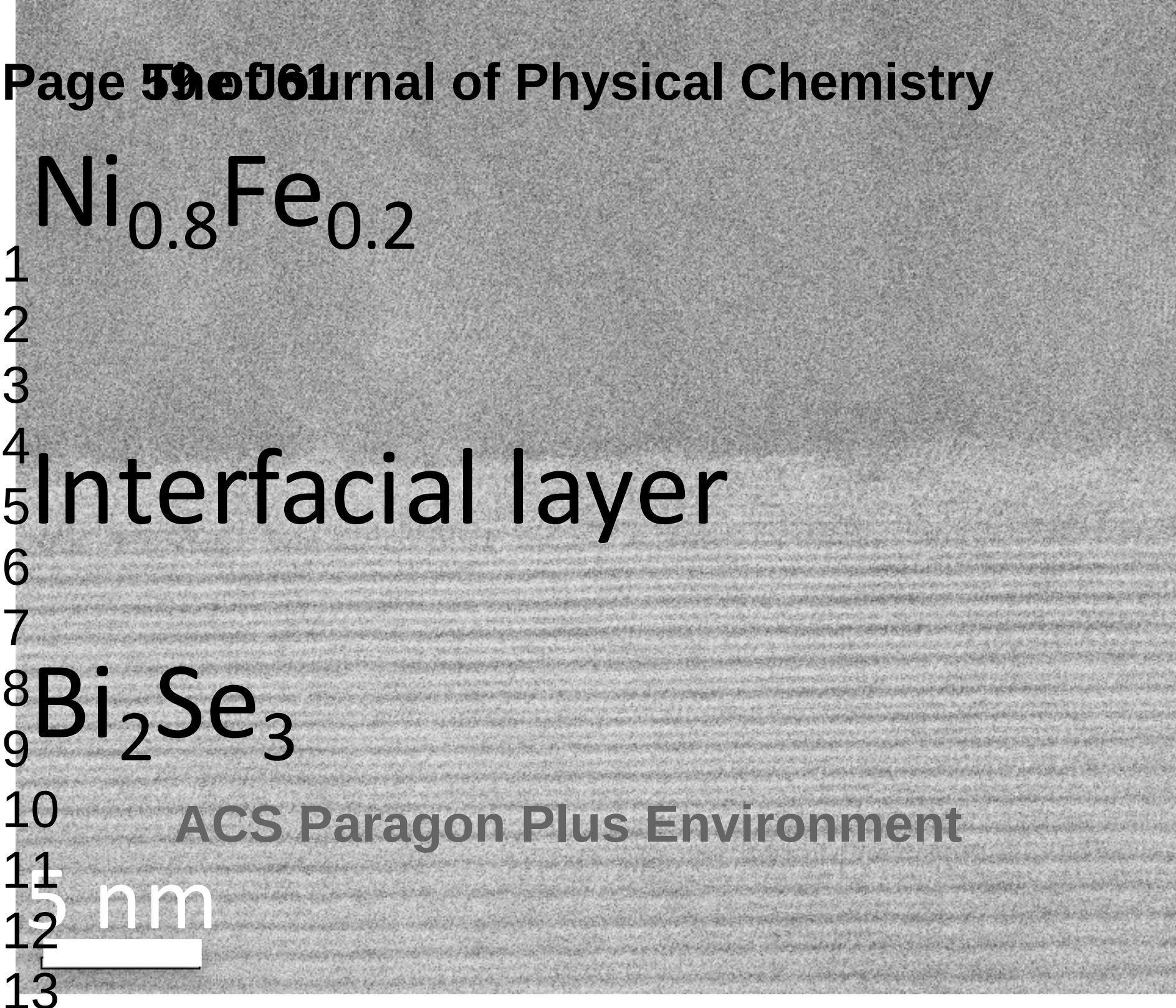
$Ni_{0.8}Fe_{0.2}$
Interfacial layer
Bi_2Se_3
ACS Paragon Plus Environment
5 nm

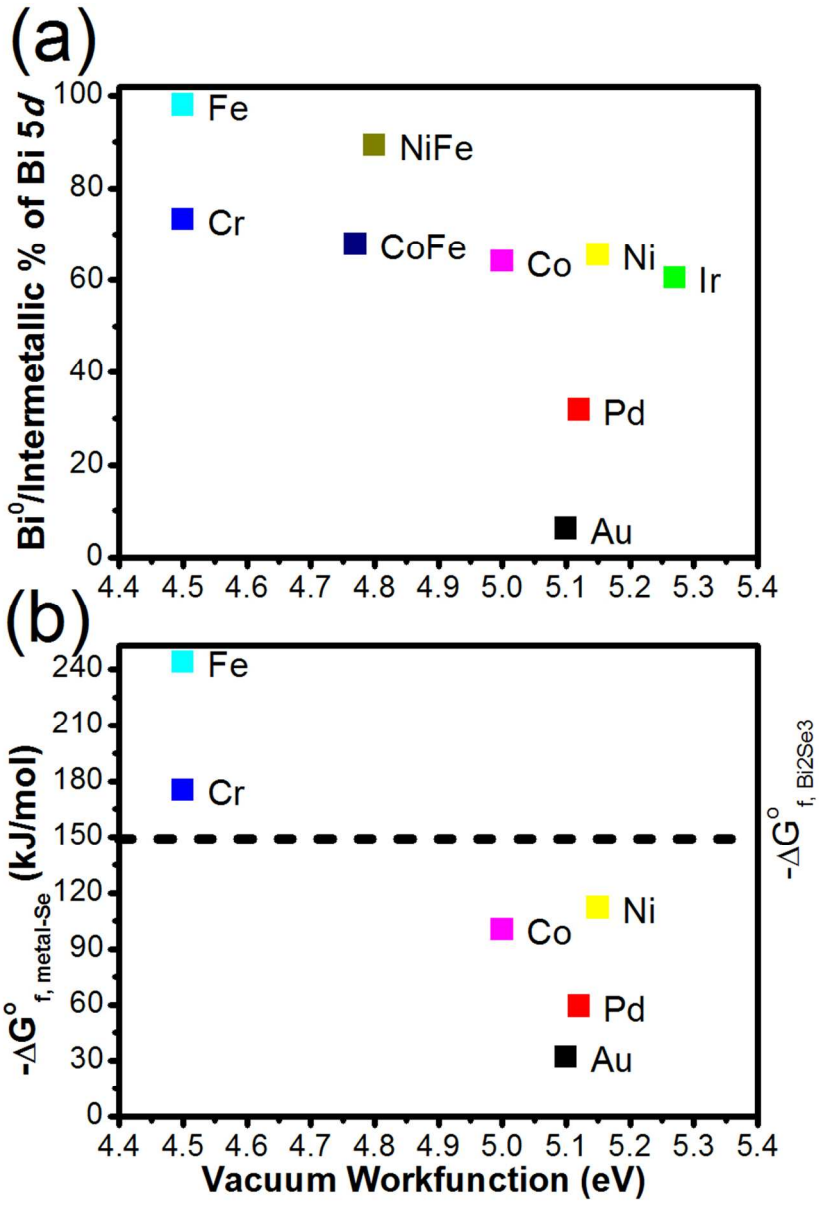

Figure 14

81x115mm (300 x 300 DPI)